



Originally published as:

Dannberg, J., Heister, T. (2016): Compressible magma/mantle dynamics: 3-D, adaptive simulations in ASPECT. - *Geophysical Journal International*, 207, 3, pp. 1343—1366.

DOI: <http://doi.org/10.1093/gji/ggw329>

# Compressible magma/mantle dynamics: 3-D, adaptive simulations in ASPECT

Juliane Dannberg<sup>1,2,\*</sup> and Timo Heister<sup>3</sup>

<sup>1</sup>*Department of Mathematics, Texas A&M University, Mailstop 3368, College Station, TX 77843-3368, USA. E-mail: dannberg@math.tamu.edu*

<sup>2</sup>*Geodynamic Modeling, GFZ German Research Centre for Geosciences, D-14473 Potsdam, Germany*

<sup>3</sup>*Mathematical Sciences, Clemson University, Clemson, SC 29634-0975, USA*

Accepted 2016 September 1. Received 2016 August 9; in original form 2015 November 17

## SUMMARY

Melt generation and migration are an important link between surface processes and the thermal and chemical evolution of the Earth's interior. However, their vastly different timescales make it difficult to study mantle convection and melt migration in a unified framework, especially for 3-D global models. And although experiments suggest an increase in melt volume of up to 20 per cent from the depth of melt generation to the surface, previous computations have neglected the individual compressibilities of the solid and the fluid phase. Here, we describe our extension of the finite element mantle convection code ASPECT that adds melt generation and migration. We use the original compressible formulation of the McKenzie equations, augmented by an equation for the conservation of energy. Applying adaptive mesh refinement to this type of problems is particularly advantageous, as the resolution can be increased in areas where melt is present and viscosity gradients are high, whereas a lower resolution is sufficient in regions without melt. Together with a high-performance, massively parallel implementation, this allows for high-resolution, 3-D, compressible, global mantle convection simulations coupled with melt migration. We evaluate the functionality and potential of this method using a series of benchmarks and model setups, compare results of the compressible and incompressible formulation, and show the effectiveness of adaptive mesh refinement when applied to melt migration. Our model of magma dynamics provides a framework for modelling processes on different scales and investigating links between processes occurring in the deep mantle and melt generation and migration. This approach could prove particularly useful applied to modelling the generation of komatiites or other melts originating in greater depths. The implementation is available in the Open Source ASPECT repository.

**Key words:** Numerical solutions; Dynamics of lithosphere and mantle; Dynamics: convection currents, and mantle plumes; Mechanics, theory, and modelling; Magma migration and fragmentation.

## 1 INTRODUCTION

Mantle convection and melt migration are important processes for our understanding of the physics of the Earth's interior and how it is linked to observations at the surface. Both processes have been studied in much detail individually, however, most studies of solid-state creep in the Earth's mantle such as in mantle plumes, subduction zones or mantle convection in general either do not consider melting and melt migration, or treat it in a simplified way, only computing the melting rate and extracting the melt from the model, neglecting (e.g. Gerya 2011; Sobolev *et al.* 2011; Ballmer *et al.* 2013, and

references therein) or approximating (Ruedas *et al.* 2004; Cagnioncle *et al.* 2007; Schmeling & Marquart 2008; Mittelstaedt *et al.* 2011) the physics of two-phase flow and the effects of compaction. Previous modelling studies of magma dynamics comprise a wide range of applications, such as dynamical melting of multicomponent materials (Ribe 1985), solitary waves (Barclon & Richter 1986; Simpson & Spiegelman 2011), channelling instabilities (Aharonov *et al.* 1995; Weatherley & Katz 2012), rifting (Schmeling 2010), mid-ocean ridges (Morgan 1987; Spiegelman & McKenzie 1987; Spiegelman 1996; Katz 2008, 2010), subduction related magmatism (Spiegelman & McKenzie 1987), melt shear bands in partially molten rocks with Newtonian (Stevenson 1989; Spiegelman 2003; Alisic *et al.* 2014), stress-dependent (Katz 2006; Alisic *et al.* 2016) and anisotropic (Butler 2012; Katz & Takei 2013; Takei & Katz 2015) viscosity, and magma dynamics in a host rock undergoing

\* Now at: Department of Mathematics, Colorado State University, 1874 Campus Delivery, Fort Collins, CO 80523-1874, USA.

both fracture and flow (Keller *et al.* 2013). However, the required computational effort has limited most tectonic scale time-dependent applications to 2-D, and although these models take into account the compaction of the solid matrix to allow melt to be expelled or to flow in, they treat both individual phases as incompressible and often assume their densities to be constant.

These simplifications are valid on small scales, but become more limiting when linking surface observations to the deeper mantle and studying the interaction of mantle and magma dynamics in the context of larger-scale structures such as mantle plumes, subduction zones, and mid-ocean ridges. The density of the solid phase (and hence its volume) changes by approximately 65 per cent over the depth of the whole mantle (Dziewonski & Anderson 1981), but the influence in the upper mantle is less than 20 per cent, and a large contribution results from phase transitions. The implied compressibilities of mantle melts are an order of magnitude higher, in a range of  $3.1 \times 10^{-11}$  to  $5.3 \times 10^{-11}$  Pa<sup>-1</sup> (Agee & Walker 1993; Ohtani & Maeda 2001; Suzuki & Ohtani 2003; Sanloup *et al.* 2013), implying that their volume can increase 7–11 per cent per 100 km they ascend from the melting region. Depending on melt composition, and especially for hydrous melt, higher compressibilities are possible (Matsukage *et al.* 2005; Jing & Karato 2008). For melts generated at pressures of 5 GPa (at a depth of approximately 150 km), such as in a plume with an excess temperatures of 250 K (Katz *et al.* 2003), compression curves (Ohtani & Maeda 2001) show that melt volumes can increase by up to 20 per cent from the melting depth to the surface. Moreover, changes in melt composition over time can further influence the melt volume. Hence, this volume change is especially important for melt generated in greater depths, such as komatiites.

Moreover, the geometry of geologic structures is not limited to 2-D, examples being transform faults at mid-ocean ridges, plate velocities and lateral variations in the thickness of the overlying plate when a mantle plume impinges on the base of the lithosphere, and bent subduction zones or along-trench variations of oceanic crustal thickness. The 3-D structure of these settings has implications for the processes of melt migration, focusing and distribution of melt, and eventually the associated volcanism at the surface.

Nevertheless, several numerical challenges have prevented joint modelling of coupled magma and mantle dynamics in 3-D so far: (1) Melt migration and mantle convection occur on widely different time and length scales, which makes it very difficult to study both processes together, as melt migration can only be resolved on a much higher resolution and using smaller time steps. (2) Important material properties strongly depend on temperature, pressure and porosity, leading for example to high viscosity contrasts of potentially more than five orders of magnitude often on very small length scales, which poses a challenge for iterative solvers. (3) These dependencies of the material parameters on the solution variables are strongly nonlinear, calling for advanced nonlinear solvers. All the previous points combined make it impossible to study these processes without using advanced numerical techniques and the ability to do large-scale parallel computations. We address these challenges in the following way:

(i) Adaptive mesh refinement allows us to refine the mesh where melt is present and viscosity contrasts are high, and to use a coarser mesh in regions without melt, where velocities and gradients of material properties are lower. For reaching the same accuracy overall

fewer degrees of freedom and computational resources are required compared to a model with uniform mesh.

(ii) Parallelization of the code, scaling up to 10 000s of processors makes it possible to run models with several tens of millions of degrees of freedom, allowing for large-scale models in 3-D that still resolve processes on the length scale of melt migration.

(iii) We use a linearized BDF2 time-stepping scheme (second-order accurate backward differentiation formula, see Kronbichler *et al.* 2012) with an optional Picard iteration, alternating the solution of the Stokes system and the advection systems until convergence is reached. We employ a generalized minimal residual method with a Wathen-style block preconditioner for the Stokes part of the problem, allowing for high local and global viscosity contrasts.

(iv) A careful design of material model parameters appropriate for whole mantle convection (no plasticity, limiting viscosities, ...) allows for stable computations even if the magmatic time and length scales are not fully resolved.

The implementation of melt migration is integrated into the open source mantle convection code ASPECT (Kronbichler *et al.* 2012; Bangerth *et al.* 2015), which is based on the deal.II finite element library (Bangerth *et al.* 2016). The massively parallel, adaptive computing capabilities of the underlying deal.II library (Bangerth *et al.* 2011) enable the computations done for this paper.

Here, we present our extension of ASPECT that models coupled magma/mantle dynamics in 2-D and 3-D, employing adaptive mesh refinement. It includes all of the terms of the original formulation of two-phase flow of McKenzie (1984), taking into account the compressibility of both individual phases, which makes this formulation (hereafter called fully compressible formulation) consistent also for higher pressures. Moreover, energy conservation, pressure-, temperature- and composition-dependent melt generation and latent heat effects are considered. We illustrate the effect of compressibility on melt migration (Section 4.1), and demonstrate the correctness and accuracy of the code by showcasing several benchmarks and convergence tests (Sections 4.2–4.4). Moreover, we show the effectiveness of adaptive mesh refinement using a test case that features structures expected in applications, but has an analytical solution (Section 4.5). Finally, we present 2-D and 3-D application cases in earth-like settings, including mantle plumes, global mantle convection and magmatic shear bands (Sections 4.3, 4.6 and 4.7). The code used to generate these results can be found in the repository at <https://github.com/geodynamic/aspect> and all input files to reproduce the results are available at Dannberg & Heister (2016).

## 2 PROBLEM SETUP

### 2.1 Physical model

The original ASPECT mantle convection code (Kronbichler *et al.* 2012) models the movement of solid mantle material. These computations also allow for taking into account how partially molten material changes the material properties and the energy balance through the release of latent heat. However, this does not include melt extraction or any relative movement between melt and solid. Here, we adapt ASPECT to solve additional equations describing the behaviour of silicate melt percolating through and interacting with a viscously deforming host rock. This is implemented based on the approach of Keller *et al.* (2013) in the viscous limit, extended to a compressible formulation.

Our model includes two material phases: The solid matrix (denoted with index *s*) and the fluid melt phase (denoted with index *f*).

**Table 1.** Explanation of some important symbols used in the paper.

Symbol	Quantity	Expression/Parametrization	Unit
$\phi$	Porosity		Volume fraction
$p_f$	Fluid pressure	$p_f = p_s - \frac{p_c}{1-\phi}$	Pa
$p_s$	Solid pressure	$p_s = p_f + \frac{p_c}{1-\phi}$	Pa
$p_c$	Compaction pressure	$p_c = (1-\phi)(p_s - p_f)$ $p_c = -\xi(\nabla \cdot \mathbf{u}_s)$	Pa
$\mathbf{u}_s$	Solid velocity		m yr <sup>-1</sup>
$\mathbf{u}_f$	Fluid velocity	$\mathbf{u}_f = \mathbf{u}_s - \frac{K_D}{\phi} (\nabla p_f - \rho_f \mathbf{g})$	m yr <sup>-1</sup>
$\dot{\epsilon}$	Strain rate	$\dot{\epsilon}(\mathbf{u}_s) = \frac{1}{2}(\nabla \mathbf{u}_s + \nabla \mathbf{u}_s^T)$	1 yr <sup>-1</sup>
$\eta$	Shear viscosity (solid)	$\eta \propto e^{-\alpha_\phi \phi}$	Pa s
$\xi$	Bulk viscosity (solid)	$\xi \propto \phi^{-m}$	Pa s
$\eta_f$	Shear viscosity (melt)		Pa s
$k_\phi$	Permeability	$k_\phi \propto \phi^n$	m <sup>2</sup>
$K_D$	Darcy coefficient	$K_D = \frac{k_\phi}{\eta_f}$	m <sup>2</sup> Pa <sup>-1</sup> s <sup>-1</sup>

The melt fraction  $\phi$  defines averaged quantities  $\bar{X}$  out of solid ( $X_s$ ) and fluid ( $X_f$ ) quantities:

$$\bar{X} = (1 - \phi)X_s + \phi X_f. \quad (1)$$

We start from the McKenzie equations, which are derived in appendix A of McKenzie (1984). The mass and momentum conservation for solid and fluid are:

$$\frac{\partial}{\partial t} [\rho_f \phi] + \nabla \cdot [\rho_f \phi \mathbf{u}_f] = \Gamma, \quad (2)$$

$$\frac{\partial}{\partial t} [\rho_s(1 - \phi)] + \nabla \cdot [\rho_s(1 - \phi)\mathbf{u}_s] = -\Gamma, \quad (3)$$

$$\phi(\mathbf{u}_f - \mathbf{u}_s) = -K_D(\nabla p_f - \rho_f \mathbf{g}), \quad (4)$$

$$-\nabla \cdot \left[ 2\eta \left( \dot{\epsilon}(\mathbf{u}_s) - \frac{1}{3}(\nabla \cdot \mathbf{u}_s)\mathbf{1} \right) + \xi(\nabla \cdot \mathbf{u}_s)\mathbf{1} \right] + \nabla p_f = \bar{\rho} \mathbf{g}, \quad (5)$$

where  $\rho$  is the density (with the index denoting solid or fluid phase),  $\mathbf{g}$  is the gravitational acceleration,  $\Gamma$  is the melting rate, and the other symbols are as given in Table 1. In order to eliminate the time derivatives, and under the assumption that the flow field is in equilibrium ( $\partial \rho_{s,f} / \partial t = 0$ ), we rewrite the first two equations to:

$$\frac{\partial \phi}{\partial t} + \nabla \cdot [\phi \mathbf{u}_f] = \frac{\Gamma}{\rho_f} - \frac{\phi}{\rho_f} \mathbf{u}_f \cdot \nabla \rho_f, \quad (6)$$

$$-\frac{\partial \phi}{\partial t} + \nabla \cdot [(1 - \phi)\mathbf{u}_s] = -\frac{\Gamma}{\rho_s} - \frac{1 - \phi}{\rho_s} \mathbf{u}_s \cdot \nabla \rho_s. \quad (7)$$

Now we can add eqs (6) and (7) and get

$$\nabla \cdot [\phi \mathbf{u}_f + (1 - \phi)\mathbf{u}_s] = \Gamma \left( \frac{1}{\rho_f} - \frac{1}{\rho_s} \right) - \frac{\phi}{\rho_f} \mathbf{u}_f \cdot \nabla \rho_f - \frac{1 - \phi}{\rho_s} \mathbf{u}_s \cdot \nabla \rho_s. \quad (8)$$

To eliminate the fluid velocity  $\mathbf{u}_f$  from the equations, we replace it by using Darcy's law (eq. 4):

$$\phi \mathbf{u}_f = \phi \mathbf{u}_s - K_D(\nabla p_f - \rho_f \mathbf{g}) \quad (9)$$

and get

$$\begin{aligned} & \nabla \cdot \mathbf{u}_s - \nabla \cdot [K_D(\nabla p_f - \rho_f \mathbf{g})] \\ &= \Gamma \left( \frac{1}{\rho_f} - \frac{1}{\rho_s} \right) - \frac{\phi}{\rho_f} \mathbf{u}_s \cdot \nabla \rho_f + \frac{K_D}{\rho_f} (\nabla p_f - \rho_f \mathbf{g}) \cdot \nabla \rho_f \\ & \quad - \frac{1 - \phi}{\rho_s} \mathbf{u}_s \cdot \nabla \rho_s. \end{aligned} \quad (10)$$

Rearranging terms, we get

$$\begin{aligned} & \nabla \cdot \mathbf{u}_s - \nabla \cdot K_D \nabla p_f - K_D \nabla p_f \cdot \frac{\nabla \rho_f}{\rho_f} \\ &= -\nabla \cdot (K_D \rho_f \mathbf{g}) + \Gamma \left( \frac{1}{\rho_f} - \frac{1}{\rho_s} \right) \\ & \quad - \frac{\phi}{\rho_f} \mathbf{u}_s \cdot \nabla \rho_f - \frac{1 - \phi}{\rho_s} \mathbf{u}_s \cdot \nabla \rho_s - K_D \mathbf{g} \cdot \nabla \rho_f \quad \text{in } \Omega. \end{aligned} \quad (11)$$

The last three terms contain gradients of the solid and fluid density, respectively, and are typically nonlinear. As densities are typically model specific input parameters, modelling of these terms has to be considered. The change in density of the solid phase is dominated by the change in static pressure, which can be written as  $\nabla p_s \approx \nabla p_{\text{static}} \approx \rho_s \mathbf{g}$ . This allows us to write

$$\frac{1}{\rho_s} \nabla \rho_s \approx \frac{1}{\rho_s} \frac{\partial \rho_{s,f}}{\partial p_s} \nabla p_s \approx \frac{1}{\rho_s} \frac{\partial \rho_s}{\partial p_s} \nabla p_{\text{static}} \approx \frac{1}{\rho_s} \frac{\partial \rho_s}{\partial p_s} \rho_s \mathbf{g} = \kappa_s \rho_s \mathbf{g}, \quad (12)$$

where  $\kappa_s$  is the isothermal compressibility of the solid. To approximate the fluid density using the fluid pressure gradient, the chosen model parameters have to be considered: If viscous compaction is large compared to Darcy drag, the fluid pressure is controlled by the melt density. On the other hand, if viscous compaction is small compared to Darcy drag, the fluid pressure is controlled by the solid density (Šrámek *et al.* 2007). This can also be expressed in terms of the compaction length  $\delta_c = \sqrt{(\xi + 4\eta/3)K_D}$ , with a small  $\delta_c$  compared to size of the melting region corresponding to the latter, and a large  $\delta_c$  corresponding to the former case. Hence, we make  $\nabla \rho_f$  a model input parameter, which can be adapted based on which force is expected to be dominant (or the user can supply the correct gradient if possible). For insights on how to choose this parameter

we refer to Section 4.1. We can now replace eq. (11) by

$$\begin{aligned} \nabla \cdot \mathbf{u}_s - \nabla \cdot K_D \nabla p_f - K_D \nabla p_f \cdot \frac{\nabla \rho_f}{\rho_f} \\ = -\nabla \cdot (K_D \rho_f \mathbf{g}) + \Gamma \left( \frac{1}{\rho_f} - \frac{1}{\rho_s} \right) \\ - \frac{\phi}{\rho_f} \mathbf{u}_s \cdot \nabla \rho_f - (\mathbf{u}_s \cdot \mathbf{g})(1 - \phi) \kappa_s \rho_s - K_D \mathbf{g} \cdot \nabla \rho_f. \end{aligned} \quad (13)$$

The original McKenzie formulation of the momentum equation (eq. 5, eqs A16–A18 in McKenzie 1984) only contains one pressure explicitly, the fluid pressure. However, for the purpose of numerically solving the system more efficiently, we can define a new variable, the compaction pressure, analogous to Keller *et al.* (2013) as

$$p_c = (1 - \phi)(p_s - p_f).$$

The viscous constitutive law for the compaction stress in the host rock (see Keller *et al.* 2013, viscous limit) is

$$p_c = -\xi(\nabla \cdot \mathbf{u}_s), \quad (14)$$

which allows us to replace the compaction term in eq. (5) by the compaction pressure:

$$-\nabla \cdot \left[ 2\eta \left( \dot{\epsilon}(\mathbf{u}_s) - \frac{1}{3}(\nabla \cdot \mathbf{u}_s)\mathbf{1} \right) \right] + \nabla p_f + \nabla p_c = \bar{\rho} \mathbf{g}. \quad (15)$$

The final set of equations are (15), (13) and (14):

$$-\nabla \cdot \left[ 2\eta \left( \dot{\epsilon}(\mathbf{u}_s) - \frac{1}{3}(\nabla \cdot \mathbf{u}_s)\mathbf{1} \right) \right] + \nabla p_f + \nabla p_c = \bar{\rho} \mathbf{g},$$

$$\begin{aligned} \nabla \cdot \mathbf{u}_s - \nabla \cdot K_D \nabla p_f - K_D \nabla p_f \cdot \frac{\nabla \rho_f}{\rho_f} \\ = -\nabla \cdot (K_D \rho_f \mathbf{g}) + \Gamma \left( \frac{1}{\rho_f} - \frac{1}{\rho_s} \right) \\ - \frac{\phi}{\rho_f} \mathbf{u}_s \cdot \nabla \rho_f - (\mathbf{u}_s \cdot \mathbf{g})(1 - \phi) \kappa_s \rho_s - K_D \mathbf{g} \cdot \nabla \rho_f, \end{aligned}$$

$$\nabla \cdot \mathbf{u}_s + \frac{p_c}{\xi} = 0.$$

The equations are solved for the solid velocity  $\mathbf{u}_s$ , the fluid pressure  $p_f$ , and the compaction pressure  $p_c$ . Without the presence of melt ( $\phi = 0$ ), the equations reduce to the standard compressible Stokes system used in ASPECT. For the material properties used in the equations, there are many different parametrizations provided in the literature, so in ASPECT these material descriptions can be set in a material model module that can be easily modified by the user, and we will use different formulations for the various models presented in this manuscript. Several of the material properties depend on the solution variables: Through the permeability, which is often parametrized as  $k_\phi = k_0 \phi^n$ , the Darcy coefficient  $K_D$  depends on the porosity. Moreover, the shear and compaction viscosities  $\eta$  and  $\xi$  can depend on the porosity, temperature, pressure, strain rate and composition. Common formulations for the dependence on porosity are  $\eta = (1 - \phi)\eta_0 e^{-\alpha_\phi \phi}$  with  $\alpha_\phi \approx 25$ – $30$  and  $\xi = \eta_0 \zeta \phi^{-n}$  with  $n \approx 1$  and  $\zeta \approx 1$ – $10$  (e.g. Katz 2008, 2010; Keller *et al.* 2013, and references therein). All of these dependencies introduce strong nonlinearities in the equations, which have to be considered when solving the system. Note that we use a three-field instead of a two-field system of equations here, based on the results of previous studies (Rhebergen *et al.* 2014, 2015) showing that the construction of a uniform preconditioner with respect to the model parameters

is difficult for the two-field formulation, while preconditioners are less sensitive to these parameters for the three-field problem.

We use Dirichlet boundary conditions for the velocity and Neumann boundary conditions for the fluid pressure:

$$\mathbf{u}_s = \mathbf{f}_1 \text{ on } \partial \Omega, \quad (16)$$

$$\nabla p_f = \mathbf{f}_2 \text{ on } \partial \Omega. \quad (17)$$

According to Darcy's law (eq. 4), prescribing the fluid pressure gradient at the boundaries also implies a melt inflow velocity  $\mathbf{u}_f$ , with  $\mathbf{u}_f - \mathbf{u}_s \propto \nabla p_f - \rho_f \mathbf{g}$ . Hence, if the lithostatic pressure gradient  $\mathbf{f}_2 = \rho_s \mathbf{g}$  is prescribed, melt can flow in or out due to variations in the dynamic pressure. On the other hand, prescribing  $\mathbf{f}_2 = \rho_f \mathbf{g}$  together with  $\mathbf{f}_1 \cdot \bar{\mathbf{n}} = 0$  leads to no in- and outflow of melt or solid. Arbitrary melt fluxes can be prescribed in addition to these options by choosing other values for  $\mathbf{f}_2$ .

Here, we do not use the visco-elasto-plastic rheology of the Keller *et al.* (2013) formulation. Hence, we do not consider the elastic deformation terms that would appear on the right hand side of eqs (15) and (14) and that include the elastic and compaction stress evolution parameters  $\xi_\tau$  and  $\xi_p$ . Moreover, our viscosity parameters  $\eta$  and  $\xi$  only cover viscous deformation instead of combining viscoelasticity and plastic failure.

In addition to the previously derived conservation equations for total mass and momentum (eqs 13–15), melt transport requires an advection equation that governs the evolution of the porosity field  $\phi$  and an equation for the conservation of energy. Under the assumption of equilibrium ( $\partial \rho_{s,f} / \partial t = 0$ ) we can write eq. (3) as

$$\rho_s \frac{\partial(1 - \phi)}{\partial t} + \nabla \cdot [\rho_s(1 - \phi)\mathbf{u}_s] = -\Gamma. \quad (18)$$

To bring this equation in the same form as the other advection equations in ASPECT, we replace the second term of the equation by

$$\nabla \cdot [\rho_s(1 - \phi)\mathbf{u}_s] = (1 - \phi)(\rho_s \nabla \cdot \mathbf{u}_s + \mathbf{u}_s \cdot \nabla \rho_s) - \rho_s \mathbf{u}_s \cdot \nabla \phi.$$

Then we use the same method as for the mass conservation and assume the change in density is dominated by the change in static pressure. This finally allows us to use eq. (12) to replace  $\nabla \rho_s / \rho_s = \kappa_s \rho_s \mathbf{g}$  and write

$$\frac{\partial \phi}{\partial t} + \mathbf{u}_s \cdot \nabla \phi = \frac{\Gamma}{\rho_s} + (1 - \phi)(\nabla \cdot \mathbf{u}_s + \kappa_s \rho_s \mathbf{g} \cdot \mathbf{u}_s). \quad (19)$$

In order to model melting and freezing of melt, we also need a solution for the temperature  $T$  and thus include an energy conservation equation in our model that includes radiogenic heat production, shear heating, adiabatic heating, and release and consumption of latent heat of melting/freezing (Rudge *et al.* 2011)

$$\begin{aligned} \phi \rho_f C_p \left( \frac{\partial T}{\partial t} + \mathbf{u}_f \cdot \nabla T \right) + (1 - \phi) \rho_s C_p \left( \frac{\partial T}{\partial t} + \mathbf{u}_s \cdot \nabla T \right) - \nabla \cdot k \nabla T \\ = \rho_s H + 2\eta(\dot{\epsilon}_s : \dot{\epsilon}_s) + \xi(\nabla \cdot \mathbf{u}_s)^2 + \frac{\phi^2}{K_D} (\mathbf{u}_f - \mathbf{u}_s)^2 \\ + \alpha T (\phi \rho_f \mathbf{u}_f \cdot \mathbf{g} + (1 - \phi) \rho_s \mathbf{u}_s \cdot \mathbf{g}) + T \Delta S \Gamma, \end{aligned} \quad (20)$$

with the shear strain rate  $\dot{\epsilon}_s = \dot{\epsilon}(\mathbf{u}_s) - \frac{1}{3}(\nabla \cdot \mathbf{u}_s)\mathbf{1}$ . This formulation assumes phase-independent parametrizations for thermal expansivity  $\alpha$  and specific heat  $C_p$ , a phase-averaged parametrization for the thermal conductivity  $k$ , and thermal equilibrium in the whole model domain.

While all terms in eq. (20) are included in the implementation in ASPECT, we decided to omit the effects of melt migration and

radiogenic heat production on the energy equation in most computations in this work for the following reasons.

First, our emphasis in this work is on the mechanical modelling and we estimate that this simplification will only have a small effect on the order of a few percent on the integrated heating rate and temperature in the model, but recognize that the influence may be much stronger locally, especially in regions where the melt fraction is high and melt velocities differ significantly from the velocity of the solid. Fast advection of heat together with the fluid flow will change the temperature distribution; and higher heating rates due to the high melt velocities in partially molten areas can provide a feedback mechanism, allowing more melt to be produced. Fig. A1 shows the differences between a model with and without the effect of melt migration on energy conservation at the example of a 1-D model of a mantle plume (with the same setup as described in Section 4.1). Temperature differences are highest at the top of the plume head: In the model where heat is advected by melt, energy is transported upwards faster and the temperature gradient at the top of the plume head is steeper, leading to overall higher average temperatures in the plume head. The maximum plume excess temperature is not changed. Hence, in applications where local temperature, heating processes or the maximum melt fraction are central, these additional heating mechanisms should be included.

Second, a potential issue with including the terms is that  $\mathbf{u}_f$  is not a primal variable in our discretization, but is computed as a postprocess using eq. (9) based on Darcy's law, which contains the gradient of  $p_f$ . As a consequence,  $\mathbf{u}_f$  is less accurate than other variables as can be seen in the numerical convergence tests (we indeed observe roughly linear convergence for  $\mathbf{u}_f$ ).

By neglecting the effects of melt migration and radiogenic heat production on the energy equation in the presented models – except for the latent heat of melting and freezing  $T\Delta S\Gamma$ , which is determined by the entropy change  $\Delta S$  upon melting the material completely and the melting rate  $\Gamma$ , we arrive at the equation:

$$\begin{aligned} \bar{\rho}C_p \left( \frac{\partial T}{\partial t} + \mathbf{u}_s \cdot \nabla T \right) - \nabla \cdot k \nabla T \\ = 2\eta(\dot{\epsilon}_s : \dot{\epsilon}_s) + \alpha T (\mathbf{u}_s \cdot \nabla p_s) + T\Delta S\Gamma. \end{aligned} \quad (21)$$

## 2.2 Weak formulation

To apply the finite element method we need to derive the weak form of the eqs (13), (14) and (15). For details see Appendix B. The final set of equations reads: Find  $\mathbf{u}_s, p_f, p_c$  with

$$\begin{aligned} (2\eta\dot{\epsilon}(\mathbf{u}_s), \dot{\epsilon}(\mathbf{v}_s)) - \left( \frac{2}{3}\eta\nabla \cdot \mathbf{u}_s, \nabla \cdot \mathbf{v}_s \right) - (p_f, \nabla \cdot \mathbf{v}_s) - (p_c, \nabla \cdot \mathbf{v}_s) \\ = (\bar{\rho}\mathbf{g}, \mathbf{v}_s), \end{aligned} \quad (22)$$

$$\begin{aligned} -(\nabla \cdot \mathbf{u}_s, q_f) - (K_D \nabla p_f, \nabla q_f) + \left( K_D \nabla p_f \cdot \frac{\nabla \rho_f}{\rho_f}, q_f \right) \\ = - (K_D \rho_f \mathbf{g}, \nabla q_f) + \int_{\partial\Omega} q_f K_D (\rho_f \mathbf{g} - \mathbf{f}_2) \cdot \bar{\mathbf{n}} \, ds \\ - \left( \frac{1}{\rho_f} - \frac{1}{\rho_s} \right) (\Gamma, q_f) + \left( \frac{\phi}{\rho_f} \mathbf{u}_s \cdot \nabla \rho_f, q_f \right) \\ + ((\mathbf{u}_s \cdot \mathbf{g})(1 - \phi)\kappa_s \rho_s, q_f) \\ + (K_D \mathbf{g} \cdot \nabla \rho_f, q_f), \end{aligned} \quad (23)$$

$$-(\nabla \cdot \mathbf{u}_s, q_c) - \left( \frac{1}{\xi} p_c, q_c \right) = 0. \quad (24)$$

for all test functions  $\mathbf{v}_s, q_f, q_c$ .

## 3 DISCRETIZATION AND LINEAR SOLVERS

Let  $(\mathbf{u}_s, p_f, p_c) \in V^u \times V^{p_f} \times V^{p_c}$  be the continuous solutions of the weak form (22)–(24). While  $V^u = [H_0^1(\Omega)]^d$  is natural (we assume homogeneous boundary conditions for simplicity here), the choice for  $V^{p_f}$  and  $V^{p_c}$  requires more thought:

Unique solvability can only be expected with an additional normalization condition like  $\int_{\Omega} p_f = 0$ . If we assume  $K_D > 0$  at all times, the natural space for the fluid pressure would be

$$V^{p_f} = H_*^1(\Omega) = H^1(\Omega) \cap L_*^2(\Omega),$$

while for  $K_D = 0$  it reduces to  $L_*^2(\Omega) = \{q \in L^2(\Omega) \mid \int_{\Omega} q = 0\}$  and we experience a standard inf-sup condition known from the Stokes equation.

Assuming  $\xi$  is finite, the constant in the compaction pressure  $p_c$  is already uniquely determined due to (24), which is essentially an  $L^2$  projection of the divergence into  $p_c$ . The correct space here is  $V^{p_c} = L^2(\Omega)$ .

We now discretize using conforming finite elements on quadrilaterals. An example for a stable discretization is given by

$$V_h^u \times V_h^{p_f} \times V_h^{p_c} = \mathcal{Q}_k^d \times \mathcal{Q}_{k-1} \times \mathcal{Q}_{k-1} \subset V^u \times V^{p_f} \times V^{p_c}$$

with  $k \geq 2$  where  $\mathcal{Q}_k$  is the standard continuous space of tensor-product polynomials of degree  $k$  on the reference cell. For  $k = 2$  this results in the standard Taylor–Hood pair  $\mathcal{Q}_2^d \times \mathcal{Q}_1$  for both velocity/pressure pairs. For the evolution of the melt fraction, we achieve the best results when choosing elements of degree  $k - 1$  for the porosity field. In this case, the divergence of the velocity, which is contained in the advection equation as a source term, and the porosity are in the same function space, and no interpolation is necessary. This guarantees that no melt is generated for a divergence-free velocity field.

As we use stable finite elements, we do not have to impose a minimum permeability to avoid stability problems, which has been done in previous finite element magma dynamics implementations. Instead, there is a continuous transition to Stokes flow for zero porosity. Nevertheless, we have to limit the compaction viscosity for low porosities to guarantee  $\xi < \infty$ , which would technically be possible by setting  $1/\xi = 0$ , but would make eqs (23) and (24) linear dependent.

### 3.1 Linear System

Discretizing eqs (22)–(24), we obtain the linear system

$$\begin{pmatrix} \mathbf{A} & \mathbf{B}^T & \mathbf{B}^T \\ \mathbf{B} & \mathbf{N} & \mathbf{0} \\ \mathbf{B} & \mathbf{0} & \mathbf{K} \end{pmatrix} \begin{pmatrix} \mathbf{U}_s \\ \mathbf{P}_f \\ \mathbf{P}_c \end{pmatrix} = \begin{pmatrix} \mathbf{F} \\ \mathbf{G} \\ \mathbf{0} \end{pmatrix}, \quad (25)$$

where  $\mathbf{N}$  is the discretization of  $-(K_D \nabla p_f, \nabla q_f)$  in the incompressible case and  $\mathbf{K}$  is given by  $-(\frac{1}{\xi} p_c, q_c)$ . For compressible computations,  $\mathbf{N}$  also contains the non-symmetric, third term from eq. (23).

Based on the solver strategy in Rhebergen *et al.* (2015), we solve the block system (25) using flexible GMRES with the upper block triangular preconditioner (preconditioned from the right)

$$\mathbf{P}^{-1} = \begin{pmatrix} \mathbf{A} & \mathbf{B}^T & \mathbf{B}^T \\ \mathbf{0} & \mathbf{X} & \mathbf{0} \\ \mathbf{0} & \mathbf{0} & \mathbf{Y} \end{pmatrix}^{-1}.$$

For the Schur complement approximations we choose

$$\hat{\mathbf{X}} = -\frac{1}{\eta} \mathbf{M}_{p_f} - K_D \mathbf{L}_{p_f} \approx -\mathbf{B} \mathbf{A}^{-1} \mathbf{B}^T + \mathbf{N} = \mathbf{X}$$

and

$$\hat{\mathbf{Y}} = -\left(\frac{1}{\eta} + \frac{1}{\xi}\right) \mathbf{M}_{p_c} \approx -\mathbf{B} \mathbf{A}^{-1} \mathbf{B}^T + \mathbf{K} = \mathbf{Y},$$

where  $\mathbf{M}_*$  and  $\mathbf{L}_*$  are mass and stiffness matrices, respectively. While the preconditioner  $\mathbf{P}$  is only defined for constant coefficients this way, varying coefficients can be treated by pulling them into the integration for the mass and stiffness matrices in  $\hat{\mathbf{X}}$  and  $\hat{\mathbf{Y}}$ . For details see Heister & Rapin (2013); Silvester & Wathen (1994).

The approximation for  $\mathbf{A}^{-1}$  is done using an inner CG solver with a relative tolerance of  $10^{-2}$  preconditioned by Trilinos ML applied to the diagonal blocks of  $\mathbf{A}$ . The Schur complement solves for  $\hat{\mathbf{X}}^{-1}$  and  $\hat{\mathbf{Y}}^{-1}$  are also done using CG preconditioned by a block ILU(0).

## 4 NUMERICAL RESULTS

In the following, we will demonstrate the accuracy and versatility of our code at the example of a number of benchmark cases and relevant setups for coupled magma/mantle dynamics applications. The ASPECT code, including all presented modifications, is available at <https://github.com/geodynamic/aspect> and all input files to reproduce the results are available at Dannberg & Heister (2016). The computations were done with ASPECT version 1.5.pre sha1 #dfe0bcc70b251ecbf8aed105e1c4d5d75206bf42.

### 4.1 1-D adiabatic upwelling

To demonstrate the effect of compressibility and the choice of approximation for the fluid pressure gradient, we here present 1-D models of typical applications of coupled magma–mantle dynamics: a mid-ocean ridge and a mantle plume. For both setups, inflow at the bottom of the domain is prescribed with a fixed velocity and temperature, characteristic for the respective problem, and material is upwelling and melting adiabatically. The models are computed for four different cases: (1) approximating the material as incompressible, (2) including compressibility, assuming  $\nabla p_f = \rho_f \mathbf{g}$ , (3) including compressibility, assuming  $\nabla p_f = \rho_s \mathbf{g}$ , (4) including compressibility, assuming  $\nabla p_f = \bar{\rho} \mathbf{g}$ . The choice of approximation affects compression and expansion of melt; and comparing the fluid pressure gradients and melt volumes in these models allows us to estimate which approximation is suitable for which application, and how big differences between the formulations are.

Both models start from an adiabatic temperature profile: For the mid-ocean ridge, potential temperature and inflow velocity are 1600 K and 5 cm yr<sup>-1</sup>, respectively; for the mantle plume these parameters are 1850 K and 1.5 m yr<sup>-1</sup>, which corresponds to the inflow velocity obtained from 2-D models with an open bottom boundary for a plume with the same excess temperature and material properties (Section 4.6). The top boundary is open in both models, so

that—in accordance with mass conservation—the outflow velocity at the top depends on melt volume changes due to compressibility. All material parameters can be found in Table 3.

The mid-ocean ridge model extends to a depth of 100 km and we let it evolve until it reaches steady state. We then compare the fluid pressure gradient in the incompressible model (which does not make any assumptions about the fluid pressure) to the products  $\rho_f \mathbf{g}$ ,  $\rho_s \mathbf{g}$  and  $\bar{\rho} \mathbf{g}$  in the same model (Fig. 1, top left); and we find that for the mid-ocean ridge, the product of bulk density and gravity seems to be a good approximation for the fluid pressure gradient. As long as melt is far away from boundary layers and can be extracted easily, buoyancy forces are balanced by Darcy drag, and viscous compaction forces are negligible. This is what Šrámek *et al.* (2007) define as the Darcy equilibrium, and in this case eq. (5) becomes  $\nabla p_f = \bar{\rho} \mathbf{g}$ : The fluid pressure is controlled by the bulk density. Note that in previous studies (such as Šrámek *et al.* 2007), this approximation is mostly discussed in the limit of small porosity, where it simplifies to  $\nabla p_f = \rho_s \mathbf{g}$ .

The plume model extends to a depth of 300 km, and we let it develop until the plume approaches the upper model boundary (so the model corresponds to a plume reaching the base of the lithosphere). The same analysis of the fluid pressure gradient (Fig. 1, top centre) shows that this case, where melt fractions are higher and the model is not in steady state, has a more complicated behaviour. In the stable plume tail, melt can segregate upwards easily, and we can assume Darcy equilibrium. Hence, the product of bulk density and gravity is still a good approximation for the fluid pressure gradient. However, in the plume head, where melt segregation is limited by viscous dilation/compaction of the high-viscosity solid matrix above the melting region, the Darcy approximation is not valid. Instead, the flow regime is close to what Šrámek *et al.* 2007 call the viscogravitational equilibrium: buoyancy is balanced by viscous compaction forces, so that the viscous resistance of the solid limits melt ascent, and the difference between solid and melt velocity becomes small. In this case, eq. (4) reduces to  $\nabla p_f = \rho_f \mathbf{g}$  and the fluid pressure is controlled by the melt density.

The corresponding porosity profiles for mid-ocean ridge and plume model are shown for comparison (Fig. 1, top right). As for the region in the mantle plume where porosity is highest (the plume head), and hence the effect of melt volume changes are largest,  $\nabla p_f = \rho_f \mathbf{g}$  seems to be a good approximation, this relation is the one we choose for our 2-D and 3-D plume models in Section 4.6. However, in general it depends on the model setup which approximation is most suitable, and for most applications of coupled magma/mantle dynamics choosing  $\nabla p_f = \bar{\rho} \mathbf{g}$  is a reasonable approach.

Note that in the plume model shown above, the porosity is above the disaggregation threshold, and it is debatable if the implemented equations still hold in this case. However, the general trend shown here is also valid for much smaller porosities. We exaggerated the value for the porosity to show an extreme for how far the fluid pressure can deviate from the approximation  $\nabla p_f = \bar{\rho} \mathbf{g}$ . In most realistic models, the values will be closer together and the problem will be smaller than shown here.

In addition to estimating the fluid pressure gradient, we also compute how the melt volume changes over time in the limit of the different approximations for  $\nabla p_f$  (Fig. 1, bottom). For the mid-ocean ridge model, which is in steady state, we take the melt flux  $\phi \mathbf{u}_f$  plotted over depth as a measure for the melt volume. For the mantle plume model, we integrate the melt volume over time. In the absence of melting or freezing, and without considering the

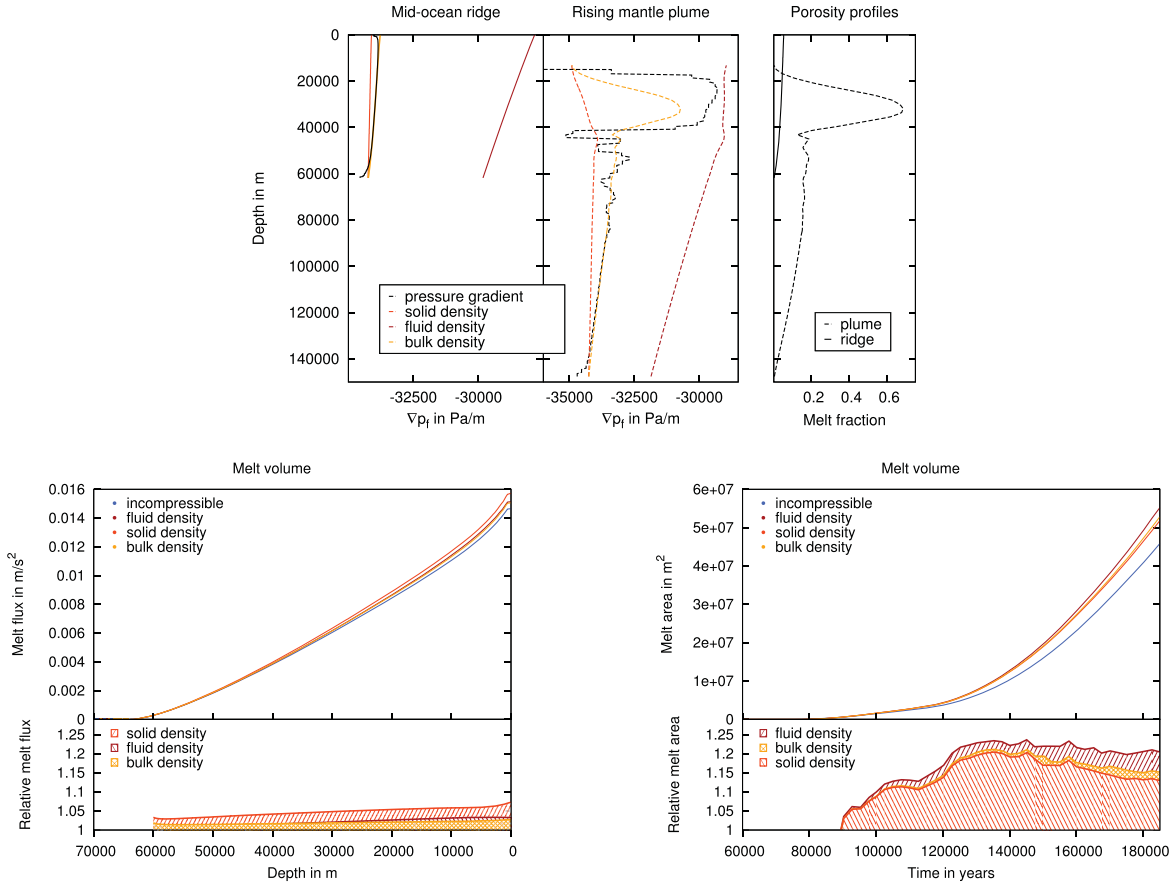


**Figure 1.** The effect of the fluid pressure gradient on melt volume changes in 1-D models of steady-state upwelling, representing the flow beneath a mid-ocean ridge, and the evolution of a rising high-temperature anomaly, such as generated by a mantle plume. Top: the left panel shows the fluid pressure gradients where melt is present in the 1-D models (black lines), together with conceivable approximations for this gradient, that is, the product of fluid density and gravity (dark red lines), the product of solid density and gravity (light red lines), and the product of bulk density and gravity (yellow lines). The right panel shows the porosity distribution in these models. All properties are shown for steady state for the ridge model, and just before the melting region reaches the upper boundary of the domain for the plume model. Bottom left: melt flux in 1-D models of a mid-ocean ridge. The melt flux in compressible models using different approximations for the fluid pressure gradient (as above) is compared to the melt flux in an incompressible model (blue line). The top panel shows profiles of the absolute melt flux, and the bottom panel shows the melt flux ratio between the different compressible models and the incompressible model. Bottom right: melt volume in 1-D models of a rising plume. The melt volume in compressible models using different approximations for the fluid pressure gradient (as above) is compared to the melt volume in an incompressible model. The top panel shows the time evolution of the absolute melt volume, and the bottom panel shows the evolution of melt volume ratio between the different compressible models and the incompressible model.

effects of compressibility, both the melt volume over time and the melt flux over depth (in a 1-D model) should be constant. Taking into account melt generation, these quantities increase as material is upwelling; and comparing them in an incompressible model and compressible models with the different approximations allows us to estimate how large the effect of compressibility on the melt volume is. This does not only include the effect of the melt volume change itself, but also its influence on material properties, such as viscosity, permeability and overall buoyancy, which in general allow a larger volume of melt to ascend faster. In the case of the steady state model, a faster ascent of melt also leads to melt leaving the model domain faster, so that less melt is present at a given point in time. Overall, this means that the approximation with the highest absolute value of the pressure gradient (in this case  $\rho_s \mathbf{g}$ ) and hence the largest melt expansion effect does not necessarily lead to the largest melt flux.

Fig. 1 (bottom) shows that in case of a mid-ocean ridge, the effect of compressibility on the melt flux is generally 5 per cent or less, independent of the approximation. For a mantle plume, one the other

hand, the differences in melt volume can be more than 20 per cent, and differences between the different approximations can be on the order of 5 per cent of the total melt volume.

## 4.2 Incompressible solitary wave benchmark

The support of nonlinear solitary waves of permanent shape and constant velocity is a well-known feature of the melt migration equations (Barcilon & Richter 1986; Barcilon & Lovera 1989). The wave behaviour develops because the solid matrix is able to compact and dilate in response to variations in melt flux, and the permeability – and hence the melt flux – increases with porosity (Spiegelman 1993a). Due to the viscous resistance of the matrix to volume changes, which hinders the buoyant ascent of melt, porosity is forced to accumulate, draining melt from surrounding areas. This creates porosity minima – new obstructions for the melt flow – and leads to the growth of solitary waves (Spiegelman 1993b). This problem has become a standard for benchmarking magma migration codes (Schmeling 2000; Simpson & Spiegelman 2011; Keller *et al.*

2013); and solitary waves have been suggested as a way of magma transport in the mantle, contributing to its episodic behaviour (Scott & Stevenson 1986; Wiggins & Spiegelman 1995). For 1-D solitary waves, assuming constant shear and compaction viscosities and using a permeability law in form of

$$k_\phi = k_0\phi^3, \quad \text{implying a Darcy coefficient } K_D(\phi) = \frac{k_0}{\eta_f}\phi^3,$$

and the non-dimensionalization

$$x = \delta x' \quad \text{with the compaction length } \delta = \sqrt{K_D(\phi_0) \left( \xi + \frac{4}{3}\eta \right)},$$

$$\phi = \phi_0\phi' \quad \text{with the background porosity } \phi_0,$$

$$(\mathbf{u}_s, \mathbf{u}_f) = u_0(\mathbf{u}_s, \mathbf{u}_f)' \quad \text{with the separation flux } \phi_0 u_0 = K_D(\phi_0)\Delta\rho g,$$

$$t = \frac{\delta}{u_0} t',$$

there is an analytical solution for the shape of the solitary wave, which can be written in the implicit form:

$$x(\phi') = \pm(A + 0.5) \times \left[ -2\sqrt{A - \phi'} + \frac{1}{\sqrt{A - 1}} \ln \frac{\sqrt{A - 1} - \sqrt{A - \phi'}}{\sqrt{A - 1} + \sqrt{A - \phi'}} \right],$$

with  $A > 1$  being the non-dimensional amplitude of the wave (Barcilon & Richter 1986). When scaled back to physical units, this equation describes a wave with the amplitude  $A\phi_0$  propagating with a fixed shape and constant phase speed  $c = u_0(2A + 1)$  in a uniform porosity ( $\phi = \phi_0$ ) background. This is only valid in the limit of small porosity  $1 - \phi_0 \sim 1$ .

For running this 1-D benchmark problem, we use a pseudo-1-D profile with only a few elements in the horizontal direction and a vertical extension of 400 m, chosen in such a way that the deviation from background porosity  $\phi/\phi_0 - 1 < 10^{-7}$ . The resolution in this direction is varied as multiples of two of the coarsest grid with  $n_z = 160$ , resulting in a resolution of 2.5 m ... 0.3 m. We apply the negative phase speed of the solitary wave  $\mathbf{u}_s = -c\mathbf{e}_z$  as velocity boundary condition, so that the wave will stay at its original position while the background is moving, and set the end time of the model to  $t = 6 \times 10^6$  years to allow the soliton to propagate five times its width. The parameters used for the model are taken from Keller *et al.* (2013) and are given in Table 2. Fig. 2 displays the shape of the solitary wave for both porosity and compaction pressure in the final time step for different models as well as the analytical solution.

We evaluate the accuracy of our model results by comparing both the phase speed and the shape of the wave after the model runtime to this analytical solution. In order to do this, we calculate the deviation of the position of the computed wave from the analytical solution (the phase shift  $\Delta z$ ). This is done by averaging over the distance between points with the same porosity in both solutions:

$$\Delta z = \sum_{\phi=\phi_0}^{A\phi_0} \frac{z_{\text{num}}(\phi) - z_{\text{ana}}(\phi)}{n}.$$

We can then use the phase shift to calculate the phase speed error

$$e_c = \left| \frac{c_{\text{num}}}{c_{\text{ana}}} - 1 \right|$$

**Table 2.** Parameters and scaling used for the solitary wave benchmark.

Symbol	Expression
$\xi$	$10^{20}$ Pa s
$\eta$	$10^{20}$ Pa s
$\eta_f$	100 Pa s
$\rho_{s0}$	$3000 \text{ kg m}^{-3}$
$\rho_{f0}$	$2500 \text{ kg m}^{-3}$
$k_0$	$5 \times 10^{-9} \text{ m}^2$
$\phi_0$	$10^{-3}$ (convergence tests)
$A$	$2.5 \times 10^{-4} - 2 \times 10^{-3}$ (porosity-dependence)
$g$	10
$K_D(\phi_0)$	$10 \text{ m s}^{-2}$
$\delta_0$	$5 \times 10^{-14} \text{ m}^3 \text{ s kg}^{-1}$
$u_0$	3.41565 m
$c$	$2.5 \times 10^{-13} \text{ m s}^{-1} = 7.8894 \times 10^{-6} \text{ m yr}^{-1}$
CFL	1, 0.5, 0.25, 0.125
$n_z$	160, 320, 640, 1280
resolution	2.5 m, 1.25 m, 0.625 m, 0.3125 m

and the porosity and pressure shape errors

$$e_\phi = \frac{\|\phi_{\text{num}}(z) - \phi_{\text{ana}}(z - \Delta z)\|_2}{A},$$

$$e_p = \frac{\|p_{c_{\text{num}}}(z) - p_{c_{\text{ana}}}(z - \Delta z)\|_2}{A_p}.$$

Fig. 3 illustrates the time evolution of these errors for simulations with different resolutions and time step sizes. After an initial transient stage, the shape and phase speed errors remain constant. This demonstrates that the code is able to capture the expected behaviour of a solitary wave that moves with a constant phase speed without changing its shape. However, the errors do not seem to converge to zero with increasing resolution. This is expected, as solitary waves are the solution of a simplified formulation of the porous flow equations that is only valid in the limit of small porosity. To show how the solution depends on the amplitude of the wave  $A$  and the background porosity  $\phi_0$ , we performed a series of models with the same parameters as given in Table 2, but varying  $\phi_0$ , and accordingly changed the reference permeability, background velocity and maximum porosity  $A\phi_0$  to retain the same non-dimensional problem, only modifying the scaling. The results (Fig. 4) show that all errors decrease with decreasing porosity. This is also visible in Fig. 2, where the shape of the solitary wave approaches the one of the analytical solution for small wave amplitudes. The results show no dependence on time step size (Fig. 3), and we attribute this to the fact that the position of the solitary wave – and the numerical solution for each time step – only changes very slowly with time because we prescribe the negative wave speed at the model boundaries.

### 4.3 Magmatic shear bands

It has been suggested and shown both numerically and experimentally that shear bands are a typical feature emerging when shear is applied to a partially molten rock (Stevenson 1989; Holtzman *et al.* 2003; Spiegelman 2003; Holtzman & Kohlstedt 2007; Butler 2009, 2010; King *et al.* 2009). The instabilities develop because the viscosity of the rock is low where porosity is high, which also leads to low pressures. Melt tends to flow towards these low-pressure regions, where it accumulates (Stevenson 1989). Shear bands are predicted

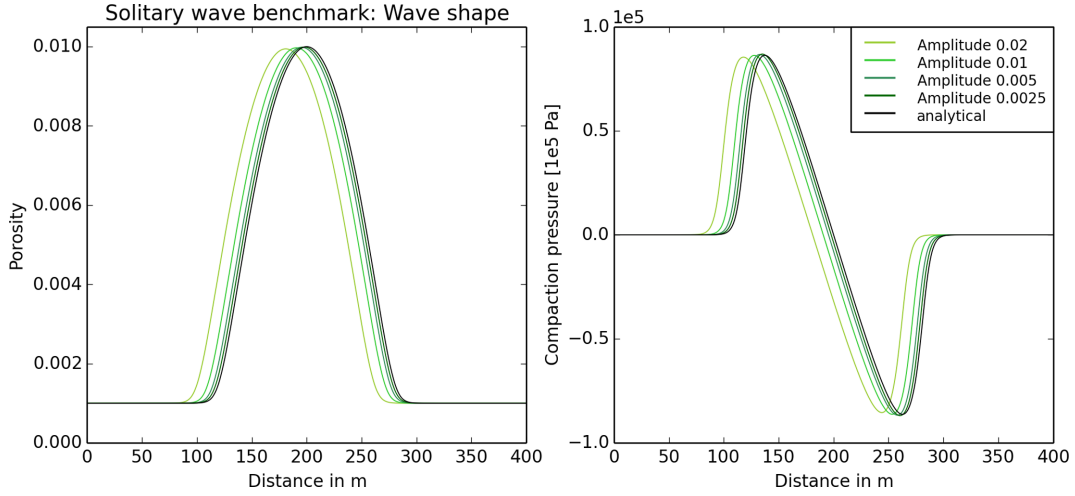


**Figure 2.** Shape of the solitary wave in porosity (left) and compaction pressure (right) for the same resolution, but different wave amplitudes, still retaining the same non-dimensional problem, after propagating five times its wavelength. The porosity is scaled according to the wave amplitude to make the plots comparable, and the end time of each model is chosen according to the phase speed of the wave (proportional to the wave amplitude) with a model time of  $t = 6 \times 10^6$  yr for  $A = 0.01$ . Both porosity and compaction pressure illustrate how the model result approaches the analytical solution with decreasing porosity.

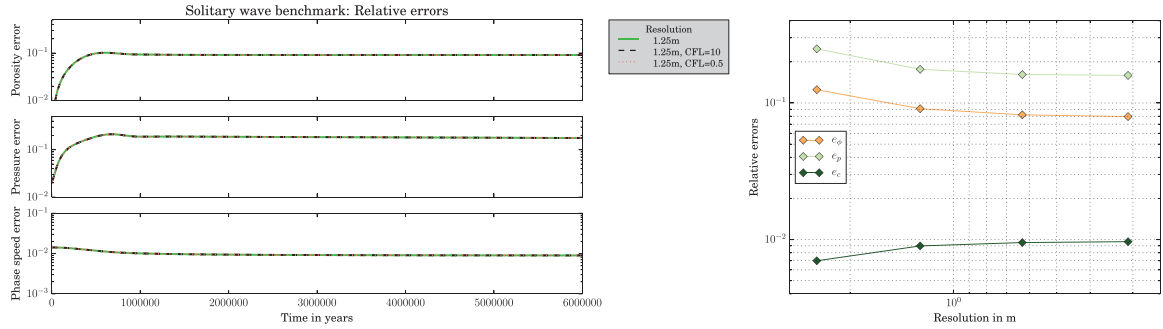


**Figure 3.** Results of temporal (left) and spatial (right) convergence tests, plotted are the errors of the porosity  $e_\phi$ , compaction pressure  $e_p$  and phase speed  $e_c$  relative to the 1-D analytical solution against model time and resolution, respectively. Grid resolution is chosen as multiples of two of the coarsest grid with 160 grid cells in vertical direction, corresponding to a cell size of 2.5–0.3 m or approximately 1/80–1/640 of the width of the solitary wave shape. Time-step lengths are chosen according to the CFL condition for the respective phase speed  $c$ .

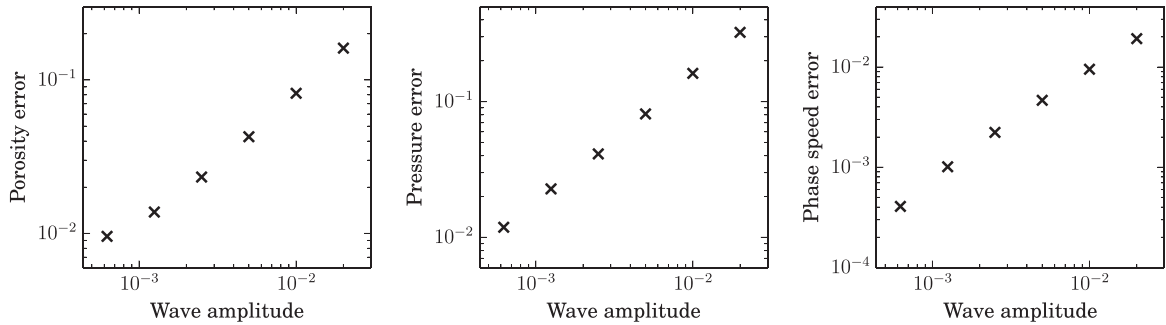


**Figure 4.** Accuracy of the solution in dependence of the solitary wave amplitude  $A\phi_0$  (and accordingly the background porosity  $\phi_0$ ). Plotted are the shape error of porosity (left), compaction pressure (middle) and the phase speed error (right) in the final time step compared to the 1-D analytical solution. All model runs are performed with a grid resolution of 0.625 m and the model end time is inversely proportional to the wave speed (proportional to the wave amplitude) with a model time of  $t = 6 \times 10^6$  yr for  $A = 0.01$ . All errors converge to zero as the porosity approaches zero.

to grow fastest under an angle of  $45^\circ$  to the orientation of highest shear stress if the rheology of the host rock is Newtonian and porosity-dependent (Spiegelman 2003), but can develop at much smaller angles in case of a combination of porosity-dependent and power-law viscosity (Katz 2006) or in case of anisotropic viscosity (Takei & Holtzman 2009; Butler 2012; Katz & Takei 2013; Takei & Katz 2013, 2015). We present shear band models for both viscos-

ity formulations, analogous to the setup described in Spiegelman (2003), Alisic *et al.* (2014) and Katz & Takei (2013) for Newtonian rheology and in Katz (2006) for power-law rheology.

The model geometry is a  $4 \text{ mm} \times 1 \text{ mm}$  2-D box periodic in the horizontal direction, starting from a background porosity  $\phi_0 = 0.05$  with small perturbations. A constant horizontal velocity  $\mathbf{u}_s$  in opposite directions is applied at the top and bottom boundaries,

**Table 3.** Parameters and scaling used for the shear bands, plume and global convection model.

Quantity	Shear bands model	Plume/ridge models	Global convection model
$\xi_0$	$1.41176 \times 10^8$ Pa s	$5 \times 10^{19}$ Pa s	$10^{19}$ Pa s
$\eta_0$	$1.41176 \times 10^7$ Pa s	$5 \times 10^{18}$ Pa s	$5 \times 10^{21}$ Pa s
$\eta_f$	100 Pa s	10 Pa s	10 Pa s
$\rho_{s0}$	$3000 \text{ kg m}^{-3}$	$3400 \text{ kg m}^{-3}$	$3400 \text{ kg m}^{-3}$
$\rho_{f0}$	$3000 \text{ kg m}^{-3}$	$3000 \text{ kg m}^{-3}$	$3000 \text{ kg m}^{-3}$
$k_0$	$5 \times 10^{-9} \text{ m}^2$	$5 \times 10^{-9} \text{ m}^2$	$10^{-8} \text{ m}^2$
$n_{\text{dis}}$	1 (Newtonian case) 6 (Power-law case)	–	–
$\phi_0$	0.05	0.05	$-(\xi \sim e^{\alpha\phi})$
$\alpha$	–1 (Newtonian case) –162 ( $\alpha/n_{\text{dis}} = -27$ )	–10	–10
$\beta$	–	5	7
$\alpha_{\text{thermal}}$	–	$3.5 \times 10^{-5} \text{ K}^{-1}$	$2 \times 10^{-5} \text{ K}^{-1}$
$T_{\text{ref}}$	–	1600 K	1600 K
$k_{\text{thermal}}$	–	$4.7 \text{ W m}^{-1} \text{ K}^{-1}$	$4.7 \text{ W m}^{-1} \text{ K}^{-1}$
$\kappa_s$	–	$3.2 \times 10^{-12} \text{ Pa}^{-1}$	$4.2 \times 10^{-12} \text{ Pa}^{-1}$
$\kappa_f$	–	$3.8462 \times 10^{-11} \text{ Pa}^{-1}$	$1.25 \times 10^{-11} \text{ Pa}^{-1}$
$\frac{\partial \kappa_f}{\partial p}$	–	1.6	0
X extent	0.004 m	600 km	8700 km
Z extent	0.001 m	300 km	2900 km
$\mathbf{u}_s$	$(\pm 3.2 \times 10^3 \text{ m yr}^{-1}, 0)$	–	–
$\gamma$	1	–	–
CFL	1	1	1
$n_x$	128, 256, 512, 1024, 2048	adaptive (128–512)	adaptive (64–512)

and the vertical gradients of pressure and porosity are required to be zero at these boundaries.

#### 4.3.1 Plane wave melt bands with porosity-weakening

For the Newtonian case, we use a rheologic law in the form of

$$\eta(\phi) = \eta_0 e^{\alpha(\phi - \phi_0)} \quad (26)$$

with an exponent of  $\alpha = -1$ , and we parametrize the permeability as  $k_\phi = k_0 \phi^2$  and the compaction viscosity as  $\xi = \xi_0 \phi_0 / \phi$ . The boundary velocity is set to  $\mathbf{u}_s = (\pm 500 \text{ m yr}^{-1}, 0)$ . A comprehensive list of model parameters and the material description can be found in Table 3. The porosity initial condition is a sinusoidal wave of the form

$$\phi(x, y) = \phi_0 + A \cos(kx \sin \theta_0 + ky \cos \theta_0), \quad (27)$$

where  $\phi_0$  is the background porosity,  $A = 10^{-4}$  is the relative amplitude of the wave,  $k$  is the wave number and  $\theta_0$  is the initial band angle. We compute the initial growth rate of these melt bands in dependence of the band angle and the chosen wave number both analytically and numerically, using the formulation derived with linear stability analysis in Spiegelman (2003) in the form it is used for this benchmark case in Alisic *et al.* (2014):

$$\dot{s}_{\text{ana}} = -\frac{\eta_0}{\xi_0 + 4/3\eta_0} \alpha(1 - \phi_0) 2\dot{\epsilon}_{xy} \sin 2\theta_0, \quad (28)$$

$$\dot{s}_{\text{num}} = -\frac{1 - \phi_0}{A\phi_0} \nabla \cdot \mathbf{u}_s. \quad (29)$$

Here,  $\dot{\epsilon}_{xy} = 0.5 \partial u_x / \partial y = 6.4 \times 10^7 \text{ yr}^{-1}$  is the  $xy$  component of the strain rate, and  $\nabla \cdot \mathbf{u}_s$  is the velocity divergence at a porosity maximum of the wave far from the boundary. We computed this value by finding the maximum (or minimum, for band angles larger than  $90^\circ$ ) velocity divergence in the centre of the box, that is, the part where  $0.001 \text{ m} < x < 0.003 \text{ m}$  and  $4.5 \times 10^{-4} \text{ m} < y < 5.5 \times 10^{-4} \text{ m}$ .

Fig. 5 shows the dependence of the growth rate  $\dot{s}$  on the initial band angle and convergence with increasing resolution. Our models reproduce the sinusoidal dependence on  $\theta_0$  with the fastest growth at an angle of  $45^\circ$  that is predicted by linear stability analysis (Spiegelman 2003). The numerical error decreases with resolution, and the convergence order is  $\mathcal{O}(h^2)$ , as reported in Alisic *et al.* (2014). At high resolution, other effects than just the grid spacing—for example, due to linearizing the governing equations to obtain the analytical solution, or the influence of the model boundary—become more important, and the error stagnates.

#### 4.3.2 Shear bands with porosity-weakening and strain-rate-weakening

For the power-law rheology, we extend the viscosity formulation to also include a dependence on the strain rate

$$\eta(\phi, \dot{\epsilon}) = \eta_0 e^{\alpha(\phi - \phi_0)/n_{\text{dis}}} \dot{\epsilon}_{II}^{(1-n_{\text{dis}})/n_{\text{dis}}}, \quad (30)$$

with an exponent of  $\alpha/n_{\text{dis}} = -27$  for the porosity and  $n_{\text{dis}} = 6$  for the strain rate. Note that this equation differs from the one in Katz (2006) in a factor of  $1/n_{\text{dis}}$  in the porosity exponent, as a rederivation of the equation (Takei & Holtzman 2009) has shown that the porosity weakening effect decreases as  $\alpha/n_{\text{dis}}$ . We still chose to use the original value  $\alpha/n_{\text{dis}} = -27$  from Katz (2006) instead of  $\alpha = -27$  to be able to compare our results to the numerical models of Katz (2006). The permeability is parametrized using the common formulation  $k_\phi = k_0 \phi^3$  and the compaction viscosity is constant. The boundary velocity  $\mathbf{u}_s = (\pm 32 \text{ km yr}^{-1}, 0)$  leads to a strain rate of  $\dot{\epsilon} = 1.434 \text{ s}^{-1}$ .

For this model setup, the porosity field is initiated with a constant background porosity  $\phi_0 = 0.05$  and added white noise with an amplitude of 0.0005. During the model evolution, elongated melt bands develop due to the applied shear; and we measure the angle of these bands after a strain of  $\gamma = 1$  is reached (Fig. 6, top).

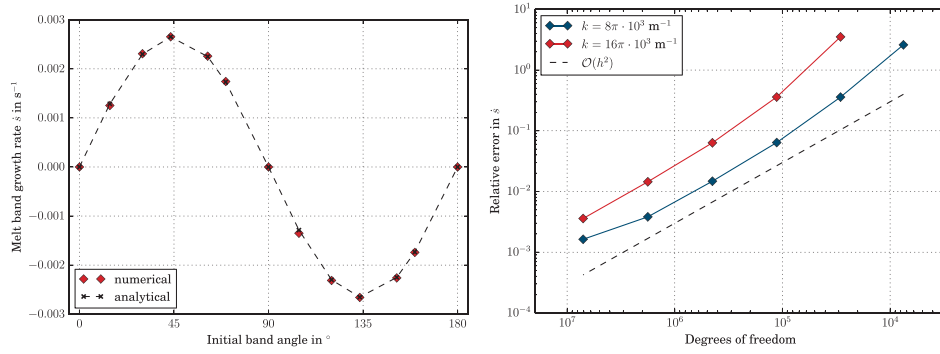


**Figure 5.** Growth rate of plane wave melt bands in a porosity-weakening material. Left: growth rate in dependence of the initial band angle  $\theta_0$  for the analytical solution and in a numerical model with a resolution of  $10^{-5}$  m ( $128 \times 512$  grid cells) and a wave number of  $k = 8\pi \times 10^3 \text{ m}^{-1}$ . Right: relative error of the growth rate  $\dot{s}$  in dependence of model resolution for melt bands with a wave number of  $k = 8\pi \times 10^3 \text{ m}^{-1}$  ( $kx_{\text{max}} = 32\pi$ ) and  $k = 16\pi \times 10^3 \text{ m}^{-1}$  ( $kx_{\text{max}} = 64\pi$ ).

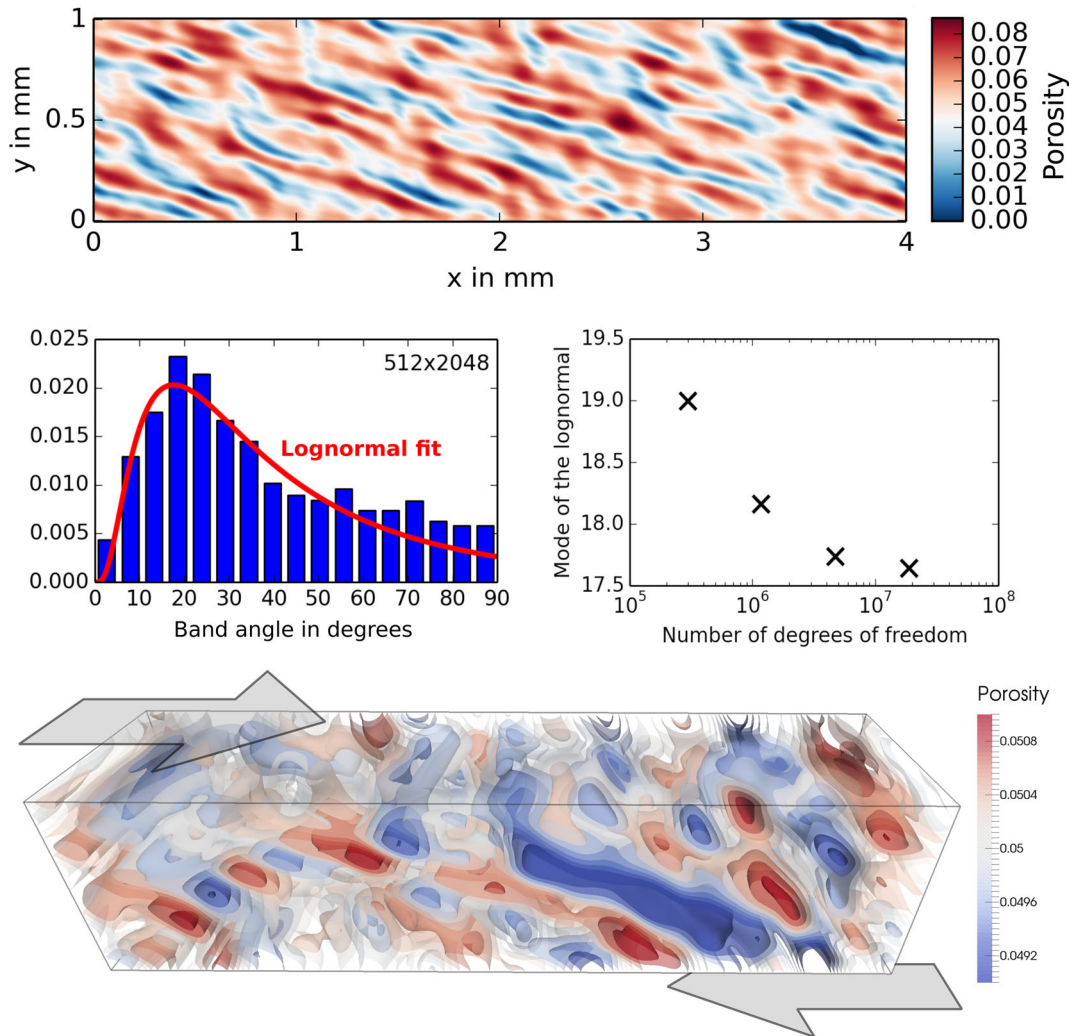


**Figure 6.** Band angle of magmatic shear bands after a strain of  $\gamma = 1$ . Top: porosity field after the final time step for a model with  $512 \times 2048$  cells. Middle left: histogram of the band angle distribution of the model shown at the top after binning in 5-degree intervals. The red line shows the best fit of a log-normal distribution to the band angle distribution. Middle right: dominant band angle (i.e. mode of the log-normal distribution shown on the left) for models with different resolution, showing convergence to a value of  $\approx 17.5^\circ$ . Bottom: shear bands in 3-D.

We apply a Fourier transform to the porosity field of the final time step and analyse the amplitude of the resulting frequencies in dependence of their angle. Fig. 6 (middle left) shows a histogram of these values binned by band angle. The average angle of the shear

bands is then computed by fitting a log-normal to the band angle distribution. Computations with varying resolutions (Fig. 6, middle right) show that the band angle converges to a value of approximately  $17.5^\circ$ , being in the range of predictions from experiments

and other numerical models, where  $15^\circ$ – $25^\circ$  to the plane of shear are reported (Katz 2006). A model of magmatic shear bands in 3-D, but otherwise identical setup (Fig. 6, bottom) reveals that the modelled shear bands are indeed planar features also in 3-D. They still emerge in a certain angle determined by the applied shear, while the white noise—initially randomly distributed in all 3-D—only modulates the concentration of porosity in the band along its extension. The model has a resolution of  $8\ \mu\text{m}$ , which corresponds to 45 million degrees of freedom, and the full model evolution is shown in Supporting Information Movie S1.

#### 4.4 Compressible convergence

To set up a 2-D test for melt transport including compressibility, we developed a new benchmark with an analytical solution, choosing the velocity, density and gravity in such a way that the laterally averaged products  $\rho_{f,s} \mathbf{u}_s$  as well as  $\rho_{f,s} \mathbf{g}$  are constant, but the divergence of the velocity is not zero:

$$\mathbf{u}_s(x, z) = (0.1e^z, -0.075e^z),$$

$$\rho_s(x, z) = 1.2e^{-z},$$

$$\rho_f(x, z) = e^{-z},$$

$$\mathbf{g}(x, z) = (0, -e^z),$$

which also leads to all the terms  $\frac{\nabla \rho}{\rho}$  being constant. The remaining material parameters are constructed to create a zero horizontal component of the fluid pressure, a vertical component that depends only on  $z$ , and to satisfy our previous assumption that  $\frac{\nabla \rho}{\rho} \approx \kappa \rho \mathbf{g}$ :

$$\eta(x, z) = \frac{1}{2}e^{2x},$$

$$\xi(x, z) = e^{-z} + \frac{2}{3}e^{2x} + 1,$$

$$K_D(x, z) = \frac{149}{45} + \frac{1}{30}e^z,$$

$$\kappa_s = \frac{5}{6},$$

$$\kappa_f = 1,$$

$$\Gamma = \frac{1}{37}e^z.$$

This leads to the following solution for the porosity, fluid pressure, compaction pressure and fluid velocity:

$$\phi(x, z) = 1 - 0.3e^z,$$

$$\nabla p_f = (0, -0.135e^z - 1),$$

$$p_c(x, z) = 0.075\xi e^{-z},$$

$$\mathbf{u}_f(x, z) = \left( 0.1e^z, -0.075e^z - 2.2\frac{K_D}{\phi}e^z \right).$$

The results are shown in Fig. 7. In the top part, velocity  $\mathbf{u}_s$  and porosity  $\phi$  are converging as expected with order  $k + 1$  in the  $L^2$  norm, except that we cannot explain why  $\mathbf{u}_s$  for  $k = 2$  is only converging quadratically (but the correct order is attained when discretizing with  $k = 3$ ). The melt velocity is computed as a postprocess from  $\mathbf{u}_s$  and the gradient of the pressure solutions, which explains the almost linear convergence order. As the melt velocity is not a variable used directly in our computations, but mainly for visualization, this is less critical. See the discussion of eq. (20) for details. The bottom

half of Fig. 7 shows convergence of the three pressures with optimal orders. Altogether, these results demonstrate the functionality and accuracy of our solver for the fully compressible formulation of two-phase flow.

#### 4.5 Adaptive convergence

To demonstrate the effectiveness of adaptive mesh refinement when applied to problems of melt migration, we have set up a test case with an incompressible, analytical solution featuring a vein of high porosity standing out against a low-porosity background (Fig. 8), and including a compaction viscosity with a Gaussian in the middle of the domain. We constructed the boundary conditions, the source term and the gravity in such a way that the solution is

$$\phi = 0.01 + 0.2 \exp(-20(x + 2z)^2),$$

$$\xi = 0.1 + 0.1 \exp(1 - 20(x^2 + z^2)),$$

$$K_D = \phi,$$

$$\mathbf{u}_s = (x, e^z - z),$$

$$p_s = 1 - z,$$

$$p_c = -\xi \nabla \cdot \mathbf{u} = -0.1e^z - 0.1e^z \exp(1 - 20(x^2 + z^2)).$$

A script to generate the constructed material parameters, source terms and boundary conditions can be found in the supporting data (Dannberg & Heister 2016).

In this example we use a refinement criterion employing a gradient jump estimator based on the porosity and the compaction pressure. An example mesh can be seen in Fig. 9 and the refinement clearly captures the region of interest for the two fields in the estimator. Note that the refinement does not match the features of the velocity or solid pressure, so we cannot expect superior performance compared to global refinement. While it would have been easy to improve the adaptive convergence by changing the setup to concentrate the features of every variable in the vein, we think this is a more realistic setup. Even then, the improvements in the error over global refinement are convincing and highlight how useful adaptive refinement in the setting of melt migration can be, see Fig. 10.

In this model global refinement requires two to four times as many degrees of freedom compared to adaptive refinement (for quantities like compaction pressure, porosity, and derived quantities like melt velocity). While quantities like solid velocity see no improvement here, the errors are very small to begin with because the field is relatively smooth compared to the melt velocity. This is likely also true for most realistic problems. For realistic models we propose to combine one of these criteria with refinement based on other solution variables or material properties such as temperature or viscosity.

#### 4.6 Melt transport in a rising mantle plume

When hot buoyant material in form of a mantle plume approaches the surface, the temperatures inside of the plume exceed the solidus and material starts to melt. We use this example as an application for our coupled magma/mantle dynamics code. We present 2-D and 3-D plume models, and employ both the incompressible and compressible formulation of two-phase flow. The model domain is a Cartesian box, extending from the Earth's surface to 300 km depth and 600 km horizontally. The initial temperature profile is adiabatic with a potential temperature of 1600 K, with a cold top thermal boundary layer corresponding to oceanic lithosphere with an age

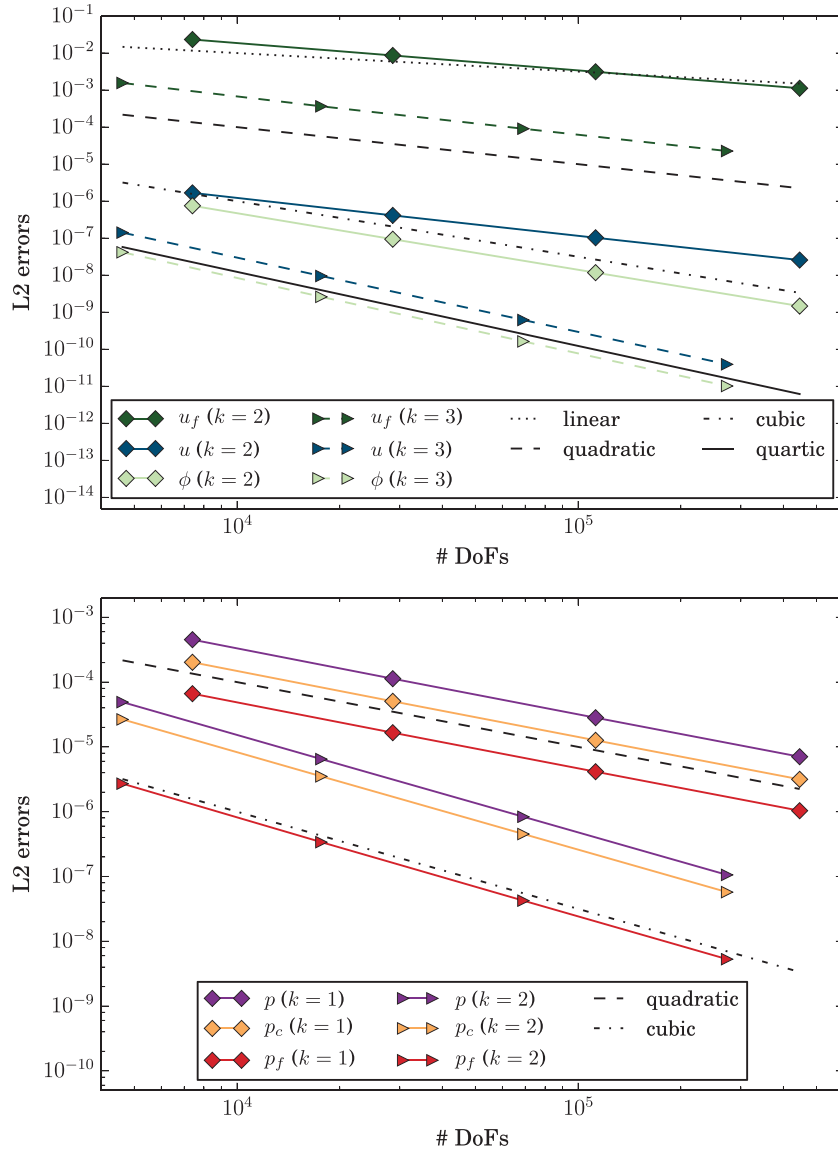


**Figure 7.** Results of spatial convergence test for different polynomial degrees  $k$  (diamonds:  $Q_2 \times Q_1$ , triangles:  $Q_3 \times Q_2$ ). Plotted are the L2 errors relative to the compressible, 2-D, analytical solution. Linear, quadratic, cubic and quartic trends are shown for reference as dotted and dashed lines.

of 10 million years and a top temperature of 293 K. A spherical perturbation of 250 K with a diameter of 80 km is added in the centre of the bottom boundary of the model to start the plume ascent. Initially, there is no porosity present in the model. The temperature boundary conditions are prescribed according to the initial values at top and bottom, and insulating at the sides; the velocity boundary conditions are free slip everywhere except for the bottom boundary layer, where the hydrostatic pressure is applied, but material is allowed to flow in and out. This leads to inflow of hot material acting as a plume tail. The rheology is purely Newtonian, but both shear and compaction viscosity are temperature- and porosity-dependent in the form

$$\eta(\phi, T) = \eta_0 e^{\alpha(\phi - \phi_0)} e^{-\beta(T - T_0)/T_0}, \quad (31)$$

$$\xi(\phi, T) = \xi_0 \frac{\phi_0}{\phi} e^{-\beta(T - T_0)/T_0}, \quad (32)$$

with exponents of  $\alpha = -5$  and  $\beta = 10$ , which are chosen lower compared to what experiments suggest to limit the viscosity contrast in the model to approximately 6 orders of magnitude. The melting

parametrization (Katz *et al.* 2003) is described in Appendix C. We apply no freezing of melt here, as we are mainly interested in how the volume of generated melt evolves over time and the related differences between the compressible and incompressible formulation. However, latent heat of melting is incorporated, with an entropy change of  $\Delta S = -300 \text{ J}/(\text{kg K})$  upon melting.

In this setting, the porosity can exceed values of 25–35 per cent, where the host rock ceases to be a connected matrix and starts to disaggregate into individual blocks and grains. It is debatable if the equations can still be applied in this limit, but it has been argued (Keller *et al.* 2013) that Darcy flow can still be a valid approximation for this type of flow, in this case describing the settling and interaction of a mush or single grains of solid in the melt phase. The permeability is then a measure for how much the relative flux of one phase is hindered by the other phase. We follow the approach of Keller *et al.* (2013) and use the parametrized permeability law

$$k_\phi = k_0 \phi^n (1 - \phi)^m \quad \text{with } n = 3 \text{ and } m = 2. \quad (33)$$

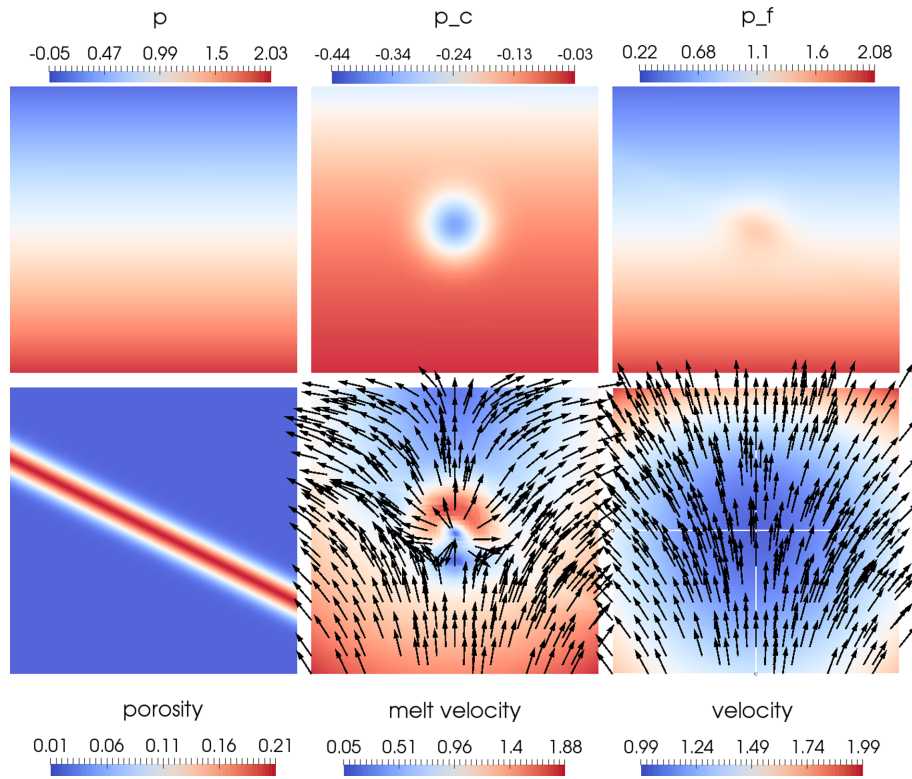


**Figure 8.** Setup of the convergence test for adaptive mesh refinement. Top row is solid pressure, compaction pressure and fluid pressure. Bottom row shows porosity, melt velocity and solid velocity. The main feature is a vein of increased porosity standing out against a low-porosity background.

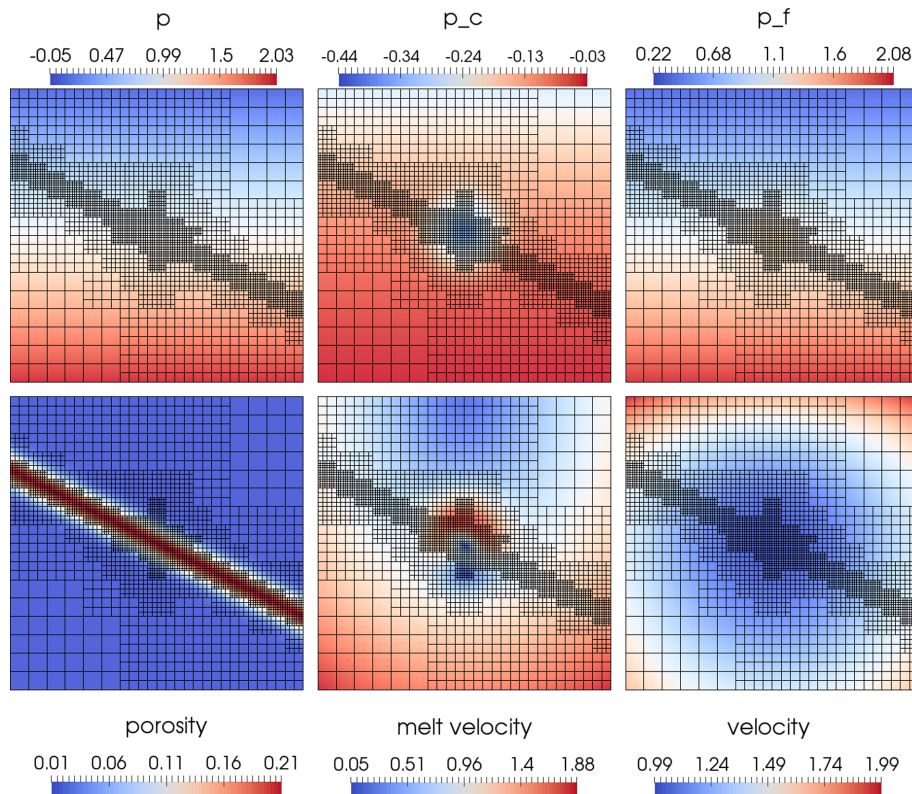


**Figure 9.** Fields like in Fig. 8, but showing the mesh refined using an error indicator based on a combination of porosity and compaction pressure gradient jumps. The algorithm clearly detects the peak in the compaction pressure and the vein and resolves them using small cells.

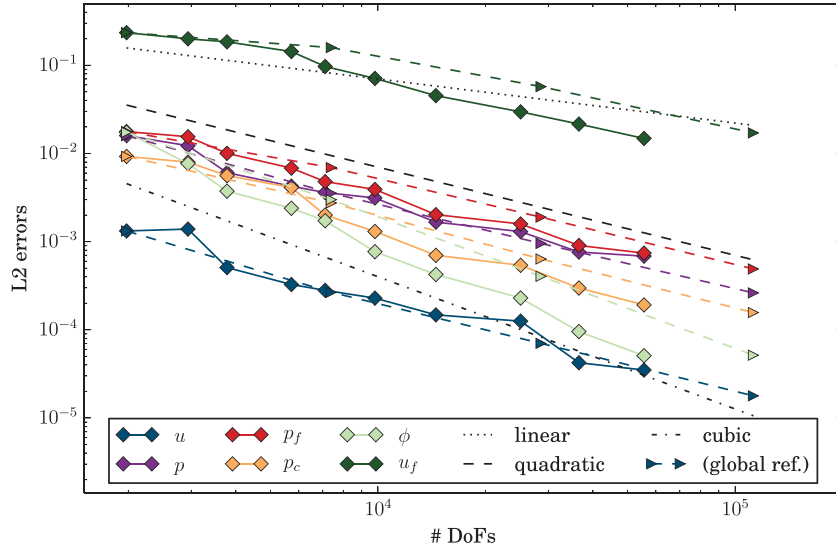


**Figure 10.** Convergence plot of L2 errors of various quantities with adaptive refinement (solid lines with diamonds) compared to global refinement (dashed lines with triangles). As expected from the refinement in the porosity vein, the errors for porosity, compaction pressure and fluid velocity are clearly superior, while other errors are comparable to global refinement. Linear, quadratic and cubic trends are shown for reference as dotted and dashed lines.

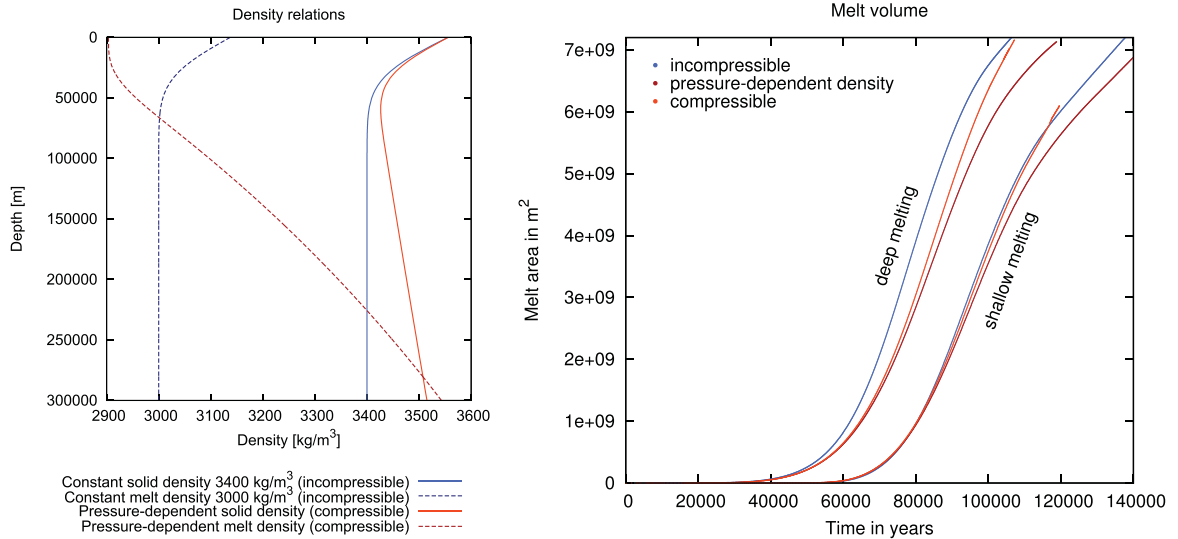


**Figure 11.** Buoyancy and melt volume in a rising mantle plume. Left: density profiles used for the different plume models: Solid lines denote solid density, dashed lines denote melt density. Colours illustrate the density formulation: Blue lines mark a density that only depends on temperature, but not on pressure; red lines mark both temperature- and pressure-dependent densities. Right: development of melt volume over time in dependence of the employed density formulation. Blue lines mark a model where both solid and melt phases are individually incompressible, and the density does not depend on pressure (blue density profiles on the left, purely incompressible formulation); dark red lines mark a model where both solid and melt phases are individually incompressible, but the density depends on pressure (red density profiles on the left, this is analogous to the extended Boussinesq approximation for Stokes flow); and light red lines mark a model where both solid and melt phases are individually compressible and the density depends on pressure (red density profiles on the left, fully compressible formulation). The two sets of lines mark different melting parametrizations, leading to melt production in different depth regions of the mantle.

Note that this approach involves a strong simplification and may in some aspects result in non-physical behaviour. In particular, as permeability goes to zero in the limit of 100 per cent porosity, the fluid is forced to move together with the solid, using the Stokes equation to compute melt velocities, which may generate shear stresses although the solid is completely disaggregated. However, it remains an open question how to accurately model magma/mantle dynamics above the disaggregation threshold. The setup we use here is chosen to demonstrate the capabilities of the code and to show differences between the compressible and incompressible formulations, and caution is recommended when transferring this model to more realistic applications.

To test the influence of considering the individual compressibility of solid and fluid on the model evolution, we designed models with three different formulations of the density parametrization (Fig. 11a):

- (i) with constant melt and solid densities  $\rho_f = 3000 \text{ kg m}^{-3}$  and  $\rho_s = 3400 \text{ kg m}^{-3}$ , only depending on temperature,
- (ii) pressure- and temperature-dependent densities, with the solid density fit to PREM (Dziewonski & Anderson 1981) and the melt density fit to data for komatiite melts (Agee & Walker 1993) using a dependency in the form  $\rho = \rho_0(1 - \alpha_{\text{thermal}}(T - T_{\text{adi}}))e^{kP}$ , but incompressible formulation of the mass and momentum conservation

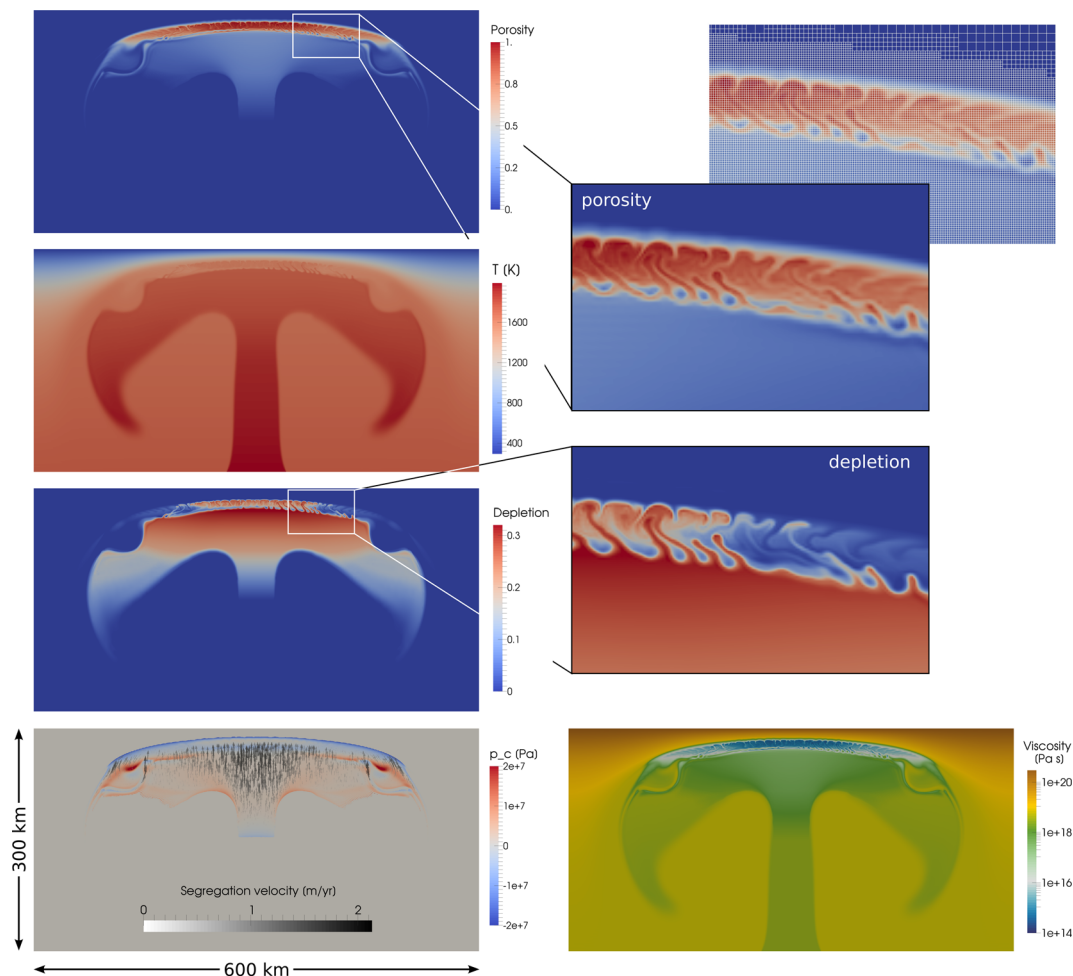


**Figure 12.** Dynamics of melt migration in a rising mantle plume. Snapshots of melt fraction (also showing the finite element mesh), depletion, temperature, compaction pressure, segregation velocity (difference between melt and solid velocity) and viscosity in the plume after a model time of  $t = 142\,000$  yr as it spreads below the lithosphere (incompressible model). During the plume ascent, melt accumulates at the top of the plume head and starts to separate from the melting region when the plume approaches the base of the lithosphere and spreads laterally. Interaction with the cold lithosphere leads to small-scale convection and mixing inside of this lens of molten material. An animation of the plume ascent is provided in Supporting Information Movie S2.

equation (analogous to the extended Boussinesq approximation for Stokes flow),

(iii) the same densities as in eq. (2), but with the fully compressible system of equations.

A comprehensive list of model parameters can be found in Table 3, and all material properties are identical to the ones used in the 1-D upwelling models presented in Section 4.1. Except for the properties mentioned above the material model is the same as described in Section 4.3.

During the model evolution, the plume ascends from the bottom of the model due to its high buoyancy. At a pressure of approximately 5 GPa material starts to melt, lowering the viscosities and further reducing the density. While the plume rises, the melt first accumulates at its top until it reaches a depth of 50 km, where the melt starts to separate from the plume head, moving further up and spreading laterally at the base of the lithosphere (Fig. 12). In agreement with previous studies of melt migration in mantle plumes with lower melt fractions (Schmeling 2000), melt segregation velocities point almost vertically upwards, and within the plume head magnitudes of melt and solid velocities are comparable. Horizontal movement occurs when melt is advected with the solid plume

material (for low melt fractions) and as it stagnates below the impermeable lithosphere in a melt-rich layer. The generated shear initiates small-scale downwellings of cold and dense lithosphere above into the low-viscosity plume material, leading to mixing in the plume head and thinning of the lithosphere. The full model evolution is shown in Supporting Information Movie S2. We evaluate the volume of generated melt over the model evolution time and compare this quantity between the different setups (Fig. 11b).

In the purely incompressible model, the density of the melt is very low, leading to a fast plume ascent and earlier melting and upwards migration of melt. In the models with pressure-dependent density, the buoyancy of the plume is smaller, and the plume rises more slowly. This explains the faster growth of melt volume for the purely incompressible model. However, there is also a volume difference between the compressible case and the incompressible, but pressure-dependent density case. As there is no difference in density parametrizations between these models, the plume buoyancy, melt generation rate and ascent velocity are identical. But as the compressible formulation considers the extension of the melt phase when it reaches lower pressures, a higher overall melt volume is reached in this model. The difference in melt volume between these two cases depends on the melt compressibility, but it is also

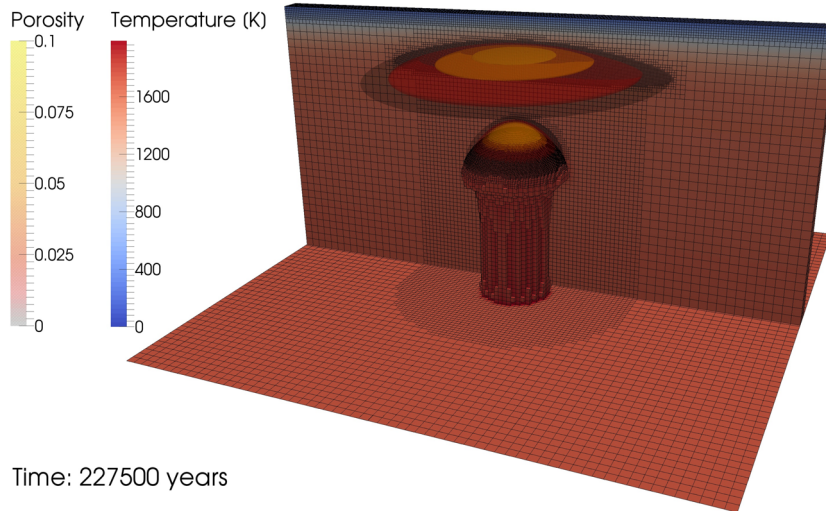


**Figure 13.** Temperature, porosity, and mesh of a snapshot of a 3-D model of melt migration in a rising mantle plume. Background colours represent temperature, contours show porosity. The mesh is refined adaptively towards the centre of the plume, in the top boundary layer and in regions where melt is present.

influenced by where and how much melt is generated, i.e. the melting parametrization. For melt generated at greater pressures, the change in density and thus the volume change is higher. For the example cases shown here it amounts to 5 per cent in the case with shallow melting and 11.4 per cent in the case with deep melting. As the models are only 2-D, these values technically represent melt areas, and not melt volumes, so that for a 3-D model an even stronger effect of compressibility (of  $\Delta V \approx \Delta A^{3/2}$ ) is expected, leading to differences of up to 18 per cent.

Fig. 13 shows a model with identical setup as in the incompressible case, but in 3-D, and illustrates how melt accumulates at the top of the rising plume head. The snapshot shows the adaptively refined mesh and demonstrates how this allows us to resolve features of interest while saving computational resources over a globally refinement mesh. For this computation, the adaptive refinement is based on a combination of refinement criteria that are evaluated every few time steps: the mesh is refined in a cylinder around the plume and in the lithosphere, and dynamically based on the presence of melt. Supporting Information Movie S3 shows the time evolution of the same model in lower resolution.

#### 4.7 Influence of melt migration on a global-scale convection model

After showcasing our implementation on a realistic example of melt migration in a rising mantle plume, we will demonstrate that with the aid of adaptive mesh refinement our software also allows it to combine models of global-scale mantle convection and melt migration. We study how melt generation and segregation impact the dynamics of such a model by comparing a classic convection model—where only the equilibrium melt fraction in dependence of temperature and pressure is computed—and a model with coupled magma/mantle dynamics, where melt is allowed to migrate. More precisely, we consider the distribution of melt, the flow field, and average velocities and temperatures.

As our focus is on the qualitative influence of melt migration on the model dynamics, we simplify the model setup to only include basic features important to study this dependence. We choose a Cartesian geometry with an aspect ratio of three and dimensions of  $2900 \times 8700$  km. The model is heated from the bottom and cooled

from the top, with no additional heat sources in the form of internal heating, latent heat or shear heating. We employ a simplified melting parametrization with a linear dependence of the solidus temperature on pressure  $p$  and depletion  $C$ , and assume that the generated melt is proportional to the temperature in excess of the solidus:

$$\phi_{\text{equilibrium}} = \frac{T - T_{\text{sol}}}{T_{\text{liq}} - T_{\text{sol}}} \quad \text{with } T_{\text{sol}} = T_{\text{sol},0} + \Delta T_p p + \Delta T_c C, \quad (34)$$

$$T_{\text{liq}} = T_{\text{sol}} + 500 \text{ K}, \quad (35)$$

$$T_{\text{sol},0} = 1300 \text{ K}, \quad (36)$$

$$\Delta T_p = 6 \times 10^{-8} \text{ K/Pa}, \quad (37)$$

$$\Delta T_c = 200 \text{ K}. \quad (38)$$

The melting rate is computed as the difference between the equilibrium melt fraction and the melt present in the model. While these melting relations are strongly simplified, they capture the qualitative influence of temperature, pressure and depletion/enrichment on the melting rate and are an appropriate approximation for studying the general model behaviour with the present melt fractions of up to 20 per cent and the dependence of melt generation and migration on the model dynamics. Whenever melt is generated in the model and migrates upwards, it leaves behind depleted material, and when the porosity present in the model exceeds the computed equilibrium melt fraction, melt freezes, creating enriched material. This change in material composition is modelled by a density change of the material proportional to enrichment/depletion, with depleted material being less dense and enriched material being denser than the surrounding mantle. In addition, porosity weakens the material as described in Section 4.6, except for the compaction viscosity, which follows an exponential dependence equivalent to the one for the shear viscosity. All model parameters can be found in Table 3.

In the classic convection model (Fig. 14, top), melt is generated by decompression melting where hot material reaches a shallow depth and partially molten areas remain relatively stationary as long as the general pattern of the flow field does not change. In the model with melt migration (Fig. 14, bottom), the same mechanism

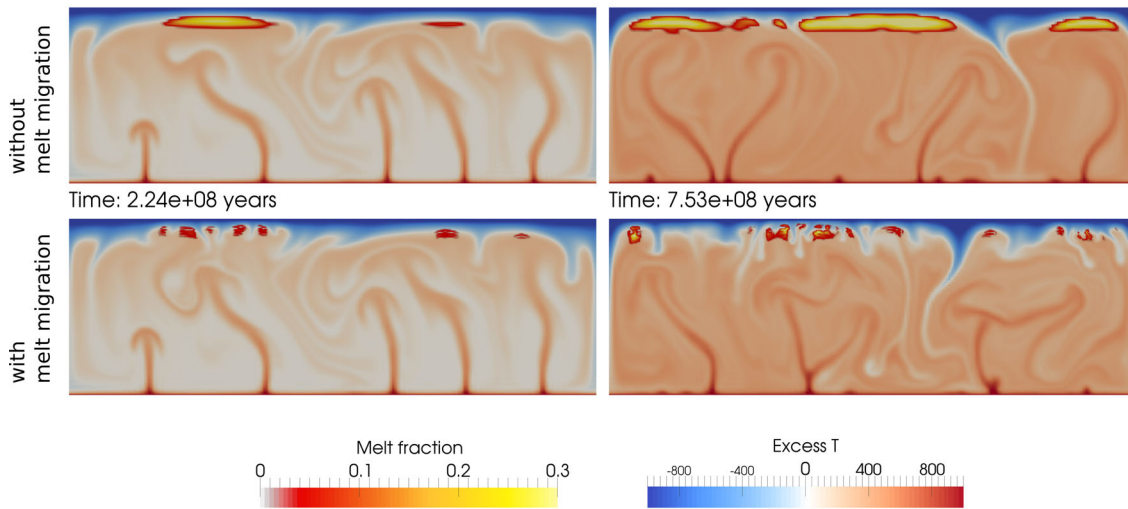


**Figure 14.** Time snapshots of temperature and melt fraction in global-scale models with melt migration. The upper row shows a model without melt migration, where the melt fraction is calculated as a post-process for the present temperature and pressure conditions (i.e. batch melting), the lower row shows a model with melt migration (and fractional melting). Columns are different points in time. The model without melt migration features broad patches of melt, generated in regions of upwelling in the model. In contrast, the model with melt migration shows several smaller patches of melt with downwellings in between, where the lithosphere is eroded due to the destabilizing effect of the high-density, crystallized material. Different average temperatures are due to the fact that the model initial conditions are not the steady-state values, but due to the model geometry (box domain and 2-D) the equilibrium conditions would not reflect realistic temperatures for the Earth.

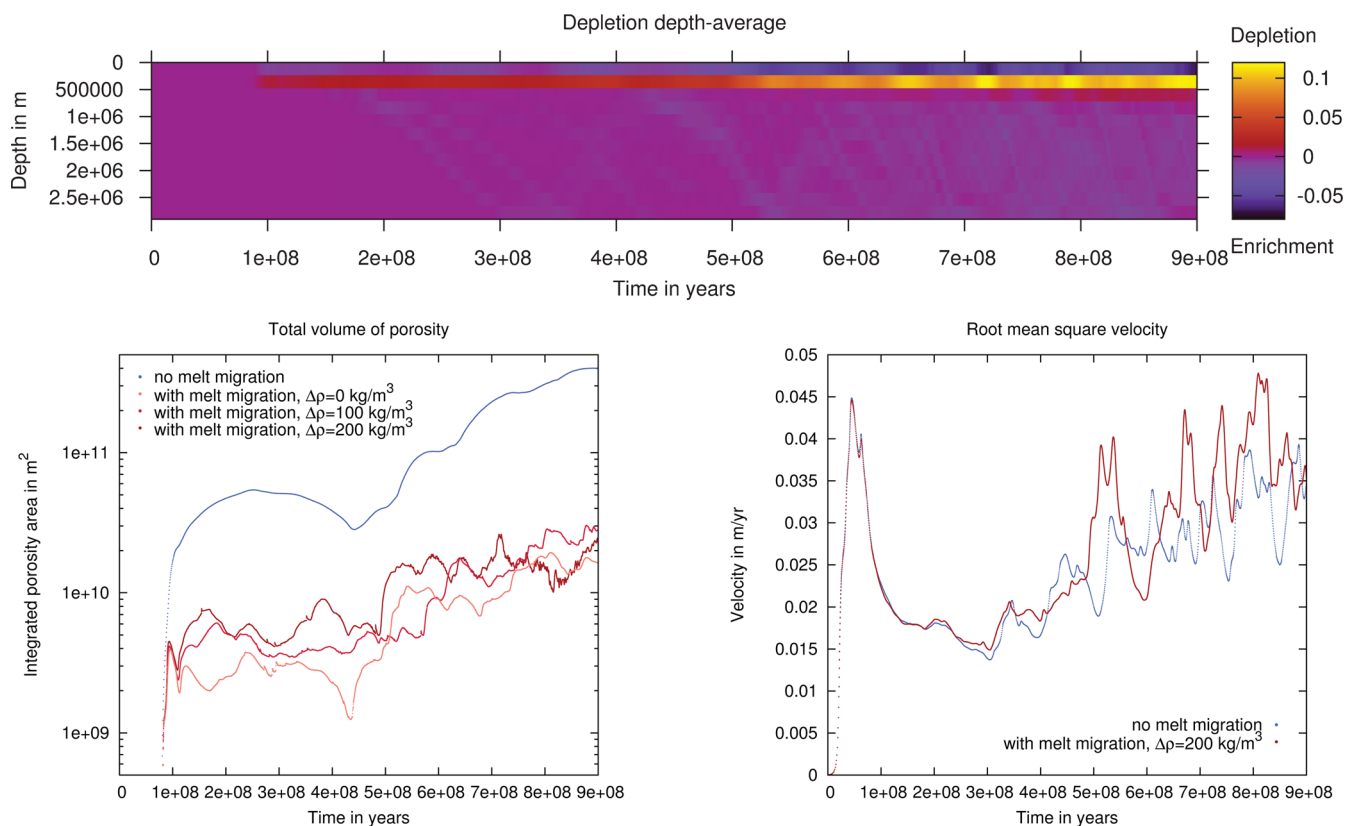


**Figure 15.** Time evolution of global models with melt migration. Top: depletion field, depth-averaged in 12 slices. Once melt starts to be generated, enriched material accumulates in the top layer, and depleted material in a layer below in 200–400 km depth. Part of the enriched material also flows downwards and is distributed over the whole model domain. Bottom left: development of the melt volume for models with (red lines) and without (blue line) melt migration, and varying density contrasts between ‘enriched’ and ‘depleted’ material. For the model without melt migration, melt volume is calculated as equilibrium melt fraction for the present temperature and pressure conditions (i.e. batch melting). Bottom right: development of the root mean square velocity for models with (red line) and without (blue line) melt migration. While the model evolution is similar in the beginning, it diverges once a significant amount of melt is generated (compare left side), and the model with melt migrations shows higher velocity peaks.

of melt generation is active, initially leading to melting in the same regions where hot material is upwelling and approaching the surface. However, as the melt migrates upwards, it reaches regions with lower ambient mantle temperatures and starts to freeze, leaving behind depleted material that is not fertile enough to generate new melt. This means that the overall melt volume is much smaller (Fig. 15, bottom left), as is expected for fractional melting in comparison to batch melting. Moreover, patches of enriched material created by freezing of melt influence the model dynamics: as it has a higher density than the surrounding mantle, cold and enriched material sinks down, initiating several small downwellings that do not occur in the model without melt migration. Fig. 15 (top) illustrates the evolution of enrichment and depletion over time: As soon as melt is generated in the model, it migrates upwards from its source, where it freezes again, creating a layer of enriched material close to the top of the model, and leaving behind a layer of depleted material below, in 200–400 km depth. In principle, even though the model is extremely simplified, these layers correspond to the Earth's crust (or at least the part of the crust generated by plumes, as there are no divergent plate boundaries in the model where oceanic crust and lithosphere would be generated) and the asthenosphere. Of course, the melt does not migrate through the previously existing cold top layer in our models and hence cannot reach the surface. However, the small-scale convection initiated by the downwellings of dense enriched, crystallized material allows for new, hot material to flow upwards, and melt intruding further upwards into the lithosphere. This is already a similar process as what is described by Sobolev *et al.* (2011) as thermo-magmatic erosion of the lithosphere by mantle plumes. The downwelling enriched material is subsequently distributed over the whole model domain (blue streaks towards the end of the time evolution in Fig. 15, top). The full model evolution is presented in Supporting Information Movie S4.

This diverging model dynamics is also visible in the root mean square velocities (Fig. 15, bottom right): during the first 250 million years both models behave almost identically, but afterwards different peaks develop in the two models. However, as the root mean square velocity is mainly influenced by upwellings instead of downwellings (due to the lower viscosities) both the average value and the frequency of peaks remain similar.

It is very likely that the model behaviour will change if a more complex melting and material behaviour is incorporated, but our model shows that already this very simple approximation of melting, together with melt migration, has a strong influence on the model dynamics, including average model velocities, predicted melt volumes and number and frequency of downwellings.

## 5 CONCLUSIONS AND OUTLOOK

In this study, we described how to implement two-phase flow in 2-D and 3-D in a finite element code with adaptive mesh refinement. The proposed formulation, which includes the compressibility of the individual solid and melt phase in addition to compaction, allows models to be extended consistently to greater depth in the Earth's mantle. The presented applications demonstrate the accuracy and efficiency of our software and its ability to capture the behaviour of melt in relevant application cases of magma/mantle dynamics on different scales, ranging from millimetres to thousands of kilometres. Simulations of mantle plumes and global convection show that including melt migration in a model significantly changes the convection pattern, and for deep melts the compressibility can have an effect of an order of 20 per cent on the computed melt volume.

The main advantages of the presented method are (1) the effectiveness of adaptive mesh refinement, allowing for higher resolution or larger model domains with the same computational resources, (2) the potential to study applications with 3-D geometries and (3) the capability to couple melt migration to processes deeper in the Earth's mantle and global mantle convection in a consistent formulation considering the compressibilities of solid and melt phase.

Despite all this, the methods described here are not sufficient to solve all conceivable models related to melt migration realistically: The focus of this study is on the coupling of magma dynamics to mantle dynamics on larger scales, and our current approach does not consider elastic and plastic deformation of the material. Hence, it does not allow for modelling of melt transport through fractures or dikes, one of the main modes of melt extraction on smaller scales such as in the lithosphere and crust (Keller *et al.* 2013). These deformation mechanisms introduce additional nonlinearities and make the problem numerically challenging, demanding the use of more efficient nonlinear solvers, ideally employing Newton's method, to be viable in 3-D.

In addition, we here concentrate on the mechanical evolution of the two-phase system, simplifying its thermal and chemical evolution and using parametrizations for calculating melting and freezing rate and the influence of melt on material properties. This approximation considers the qualitative influence of compositional changes on solidus, liquidus, density, viscosity and other material properties. However, it does not allow an accurate computation of the melt and residuum composition in a multicomponent system or the associated chemical heterogeneities generated by the melting process—which would be required for a more realistic description of the rheology of partially molten regions and a more sophisticated comparison of the model to geochemical data. Employing thermodynamic data to calculate melting rates self-consistently and keeping track of the evolution of solid and melt composition should be a goal for future modelling studies.

Finally, we assume that melt and solid are always in thermodynamic equilibrium. However, this might not be a valid approximation for all applications of porous flow in the Earth's mantle and excludes modelling disequilibrium melting such as described in Rudge *et al.* (2011). In particular, it has been suggested (Rudge *et al.* 2011) that disequilibrium transport may play an important role for reaction infiltration instabilities (Spiegelman *et al.* 2001), which lead to melt focusing and channelized flow below mid-ocean ridges.

Nevertheless, we have shown that ASPECT can be applied to a number of relevant model setups for coupled magma/mantle dynamics and that it has the potential to become a versatile and useful tool for the magma migration community.

## ACKNOWLEDGEMENTS

JD would like to thank Rene Gassmoeller for helpful suggestions regarding the implementation and for carefully and critically reading the manuscript, and Tobias Keller for many insightful discussions on coupled magma/mantle dynamics. The authors would like to thank the Isaac Newton Institute for Mathematical Sciences, Cambridge, for support and hospitality during the programme Melt in the Mantle where work on this paper was undertaken. This work was supported by EPSRC grant no EP/K032208/1. We would also like to thank Richard Katz and an anonymous reviewer for their helpful comments, which greatly helped to improve this manuscript.

Both authors were partially supported by the Computational Infrastructure for Geodynamics initiative (CIG), through the National Science Foundation under Award No. EAR-0949446 and The University of California – Davis. TH was partially supported by National Science Foundation grant DMS1522191. JD acknowledges the support of the Helmholtz graduate research school GeoSim.

Most of the computational resources were provided by the North-German Supercomputing Alliance (HLRN) as part of the project ‘Plume-Plate interaction in 3-D mantle flow – Revealing the role of internal plume dynamics on global hot spot volcanism’. Clemson University is acknowledged for generous allotment of compute time on Palmetto cluster.

## REFERENCES

- Agee, C.B. & Walker, D., 1993. Olivine flotation in mantle melt, *Earth planet. Sci. Lett.*, **114**(2–3), 315–324.
- Aharonov, E., Whitehead, J., Kelemen, P. & Spiegelman, M., 1995. Channeling instability of upwelling melt in the mantle, *J. geophys. Res.*, **100**(B10), 20 433–20 450.
- Alicic, L., Rudge, J.F., Katz, R.F., Wells, G.N. & Rhebergen, S., 2014. Compaction around a rigid, circular inclusion in partially molten rock, *J. geophys. Res.*, **119**(7), 5903–5920.
- Alicic, L., Rhebergen, S., Rudge, J.F., Katz, R.F. & Wells, G.N., 2016. Torsion of a cylinder of partially molten rock with a spherical inclusion: theory and simulation, *Geochem. Geophys. Geosyst.*, **17**(1), 143–161.
- Ballmer, M.D., Ito, G., Wolfe, C.J. & Solomon, S.C., 2013. Double layering of a thermochemical plume in the upper mantle beneath Hawaii, *Earth planet. Sci. Lett.*, **376**, 155–164.
- Bangerth, W., Burstedde, C., Heister, T. & Kronbichler, M., 2011. Algorithms and data structures for massively parallel generic adaptive finite element codes, *ACM Trans. Math. Softw.*, **38**(2), doi:10.1145/2049673.2049678.
- Bangerth, W. et al., 2015. *ASPECT: Advanced Solver for Problems in Earth's Convection*. Available at: <https://aspect.dealii.org/>.
- Bangerth, W. et al., 2016. The deal.II library, version 8.4, *J. Numer. Math.*, **24**, doi:10.1515/jnma-2016-1045.
- Barcilon, V. & Lovera, O.M., 1989. Solitary waves in magma dynamics, *J. Fluid Mech.*, **204**, 121–133.
- Barcilon, V. & Richter, F.M., 1986. Nonlinear waves in compacting media, *J. Fluid Mech.*, **164**, 429–448.
- Butler, S., 2009. The effects of buoyancy on shear-induced melt bands in a compacting porous medium, *Phys. Earth planet. Inter.*, **173**(1), 51–59.
- Butler, S., 2010. Porosity localizing instability in a compacting porous layer in a pure shear flow and the evolution of porosity band wavelength, *Phys. Earth planet. Inter.*, **182**(1), 30–41.
- Butler, S., 2012. Numerical models of shear-induced melt band formation with anisotropic matrix viscosity, *Phys. Earth planet. Inter.*, **200**, 28–36.
- Cagnioncle, A.-M., Parmentier, E.M. & Elkins-Tanton, L.T., 2007. Effect of solid flow above a subducting slab on water distribution and melting at convergent plate boundaries, *J. geophys. Res.*, **112**(B9), B09402, doi:10.1029/2007JB004934.
- Dannberg, J. & Heister, T., 2016. Supporting input files, data files, and scripts. Available at: <https://github.com/jdannberg/melt-transport-data>.
- Dziewonski, A.M. & Anderson, D.L., 1981. Preliminary reference earth model, *Phys. Earth planet. Inter.*, **25**(4), 297–356.
- Gerya, T., 2011. Future directions in subduction modeling, *J. Geodyn.*, **52**(5), 344–378.
- Heister, T. & Rapin, G., 2013. Efficient augmented Lagrangian-type preconditioning for the Oseen problem using Grad-Div stabilization, *Int. J. Numer. Methods Fluids*, **71**, 118–134.
- Holtzman, B., Groebner, N., Zimmerman, M., Ginsberg, S. & Kohlstedt, D., 2003. Stress-driven melt segregation in partially molten rocks, *Geochem. Geophys. Geosyst.*, **4**(5), 8607, doi:10.1029/2001GC000258.
- Holtzman, B.K. & Kohlstedt, D.L., 2007. Stress-driven melt segregation and strain partitioning in partially molten rocks: effects of stress and strain, *J. Petrol.*, **48**(12), 2379–2406.
- Jing, Z. & Karato, S.-I., 2008. Compositional effect on the pressure derivatives of bulk modulus of silicate melts, *Earth planet. Sci. Lett.*, **272**(1), 429–436.
- Katz, R.F., 2006. The dynamics of melt and shear localization in partially molten aggregates, *Nature*, **442**, 676–679.
- Katz, R.F., 2008. Magma dynamics with the enthalpy method: benchmark solutions and magmatic focusing at mid-ocean ridges, *J. Petrol.*, **49**(12), 2099–2121.
- Katz, R.F., 2010. Porosity-driven convection and asymmetry beneath mid-ocean ridges, *Geochem. Geophys. Geosyst.*, **11**(11), Q0AC07, doi:10.1029/2010GC003282.
- Katz, R.F. & Takei, Y., 2013. Consequences of viscous anisotropy in a deforming, two-phase aggregate. Part 2. Numerical solutions of the full equations, *J. Fluid Mech.*, **734**, 456–485.
- Katz, R.F., Spiegelman, M. & Langmuir, C.H., 2003. A new parameterization of hydrous mantle melting, *Geochem. Geophys. Geosyst.*, **4**(9), 1073, doi:10.1029/2002GC000433.
- Keller, T., May, D.A. & Kaus, B.J.P., 2013. Numerical modelling of magma dynamics coupled to tectonic deformation of lithosphere and crust, *Geophys. J. Int.*, **195**(3), 1406–1442.
- King, D.S., Zimmerman, M.E. & Kohlstedt, D.L., 2010. Stress-driven melt segregation in partially molten olivine-rich rocks deformed in torsion, *J. Petrol.*, **51**, 21–42.
- Kronbichler, M., Heister, T. & Bangerth, W., 2012. High accuracy mantle convection simulation through modern numerical methods, *Geophys. J. Int.*, **191**(1), 12–29.
- Matsukage, K.N., Jing, Z. & Karato, S.-I., 2005. Density of hydrous silicate melt at the conditions of earth's deep upper mantle, *Nature*, **438**(7067), 488–491.
- McKenzie, D., 1984. The generation and compaction of partially molten rock, *J. Petrol.*, **25**(3), 713–765.
- Mittelstaedt, E., Ito, G. & van Hunen, J., 2011. Repeat ridge jumps associated with plume-ridge interaction, melt transport, and ridge migration, *J. geophys. Res.*, **116**(B1), doi:10.1029/2010JB007504.
- Morgan, J.P., 1987. Melt migration beneath mid-ocean spreading centers, *Geophys. Res. Lett.*, **14**(12), 1238–1241.
- Ohtani, E. & Maeda, M., 2001. Density of basaltic melt at high pressure and stability of the melt at the base of the lower mantle, *Earth planet. Sci. Lett.*, **193**(1–2), 69–75.
- Rhebergen, S., Wells, G.N., Katz, R.F. & Wathen, A.J., 2014. Analysis of block preconditioners for models of coupled magma/mantle dynamics, *SIAM J. Sci. Comput.*, **36**(4), A1960–A1977.
- Rhebergen, S., Wells, G.N., Wathen, A.J. & Katz, R.F., 2015. Three-field block preconditioners for models of coupled magma/mantle dynamics, *SIAM J. Sci. Comput.*, **37**(5), A2270–A2294.
- Ribe, N.M., 1985. The generation and composition of partial melts in the earth's mantle, *Earth planet. Sci. Lett.*, **73**(2), 361–376.
- Rudge, J.F., Bercovici, D. & Spiegelman, M., 2011. Disequilibrium melting of a two phase multicomponent mantle, *Geophys. J. Int.*, **184**(2), 699–718.
- Ruedas, T., Schmeling, H., Marquart, G., Kreutzmann, A. & Junge, A., 2004. Temperature and melting of a ridge-centred plume with application to Iceland. Part I: dynamics and crust production, *Geophys. J. Int.*, **158**(2), 729–743.
- Sanloup, C., Drewitt, J.W.E., Konopkova, Z., Dalladay-Simpson, P., Morton, D.M., Rai, N., van Westrenen, W. & Morgenroth, W., 2013. Structural change in molten basalt at deep mantle conditions, *Nature*, **503**, 104–107.
- Schmeling, H., 2000. Partial melting and melt segregation in a convecting mantle, in *Physics and Chemistry of Partially Molten Rocks*, pp. 141–178, eds Bagdassarov, N., Laporte, D. & Thompson, A.B., Springer.
- Schmeling, H., 2010. Dynamic models of continental rifting with melt generation, *Tectonophysics*, **480**(1–4), 33–47.
- Schmeling, H. & Marquart, G., 2008. Crustal accretion and dynamic feedback on mantle melting of a ridge centred plume: the Iceland case, *Tectonophysics*, **447**(1–4), 31–52.

- Scott, D.R. & Stevenson, D.J., 1986. Magma ascent by porous flow, *J. geophys. Res.*, **91**(B9), 9283–9296.
- Silvester, D. & Wathen, A., 1994. Fast iterative solution of stabilised Stokes systems. Part II: Using general block preconditioners, *SIAM J. Numer. Anal.*, **31**(5), 1352–1367.
- Simpson, G. & Spiegelman, M., 2011. Solitary wave benchmarks in magma dynamics, *J. Sci. Comput.*, **49**(3), 268–290.
- Sobolev, S.V., Sobolev, A.V., Kuzmin, D.V., Krivolutsкая, N.A., Petrunin, A.G., Arndt, N.T., Radko, V.A. & Vasiliev, Y.R., 2011. Linking mantle plumes, large igneous provinces and environmental catastrophes, *Nature*, **477**(7364), 312–316.
- Spiegelman, M., 1993a. Flow in deformable porous media. Part 1. Simple analysis, *J. Fluid Mech.*, **247**, 17–38.
- Spiegelman, M., 1993b. Flow in deformable porous media. Part 2. Numerical analysis—the relationship between shock waves and solitary waves, *J. Fluid Mech.*, **247**, 39–63.
- Spiegelman, M., 1996. Geochemical consequences of melt transport in 2-d: the sensitivity of trace elements to mantle dynamics, *Earth planet. Sci. Lett.*, **139**(1), 115–132.
- Spiegelman, M., 2003. Linear analysis of melt band formation by simple shear, *Geochem. Geophys. Geosyst.*, **4**(9), 8615, doi:10.1029/2002GC000499.
- Spiegelman, M. & McKenzie, D., 1987. Simple 2-D models for melt extraction at mid-ocean ridges and island arcs, *Earth planet. Sci. Lett.*, **83**(1), 137–152.
- Spiegelman, M., Kelemen, P.B. & Aharonov, E., 2001. Causes and consequences of flow organization during melt transport: the reaction infiltration instability in compactible media, *J. geophys. Res.*, **106**(B2), 2061–2077.
- Šrámek, O., Ricard, Y. & Bercovici, D., 2007. Simultaneous melting and compaction in deformable two-phase media, *Geophys. J. Int.*, **168**(3), 964–982.
- Stevenson, D.J., 1989. Spontaneous small-scale melt segregation in partial melts undergoing deformation, *Geophys. Res. Lett.*, **16**(9), 1067–1070.
- Suzuki, A. & Ohtani, E., 2003. Density of peridotite melts at high pressure, *Phys. Chem. Miner.*, **30**(8), 449–456.
- Takei, Y. & Holtzman, B.K., 2009. Viscous constitutive relations of solid-liquid composites in terms of grain boundary contiguity: 3. Causes and consequences of viscous anisotropy, *J. geophys. Res.*, **114**(B6), doi:10.1029/2008JB005852.
- Takei, Y. & Katz, R.F., 2013. Consequences of viscous anisotropy in a deforming, two-phase aggregate. Part 1. Governing equations and linearized analysis, *J. Fluid Mech.*, **734**, 424–455.
- Takei, Y. & Katz, R.F., 2015. Consequences of viscous anisotropy in a deforming, two-phase aggregate. Why is porosity-band angle lowered by viscous anisotropy?, *J. Fluid Mech.*, **784**, 199–224.
- Weatherley, S.M. & Katz, R.F., 2012. Melting and channelized magmatic flow in chemically heterogeneous, upwelling mantle, *Geochem. Geophys. Geosyst.*, **13**(5), Q0AC18, doi:10.1029/2011GC003989.
- Wiggins, C. & Spiegelman, M., 1995. Magma migration and magmatic solitary waves in 3-D, *Geophys. Res. Lett.*, **22**(10), 1289–1292.

## SUPPORTING INFORMATION

Additional Supporting Information may be found in the online version of this paper:

**Movie S1.** Animation of the development of magmatic shear bands in 3-D in a partially molten host rock that is exposed to shearing. Setup, colours and scaling are the same as in Fig. 6 (bottom). The animation can also be found at <https://youtu.be/zOEqhaiBswU>.

**Movie S2.** Animation of the evolution of a rising mantle plume that undergoes melting. Setup, colours and scaling are the same as in Fig. 12. The animation can also be found at <https://youtu.be/aWndYbMjvVQ>.

**Movie S3.** Animation of a 3-D model of the evolution of a rising mantle plume that undergoes melting. Setup, colours and scaling are the same as in Fig. 13. The animation can also be found at [https://youtu.be/41J\\_bTF4qQE](https://youtu.be/41J_bTF4qQE).

**Movie S4.** Animation of the evolution of a global-scale mantle convection model that incorporates melting, illustrating the difference between only computing melt fractions (top) and allowing melt to migrate and influence the model behaviour (bottom). Setup, colours and scaling are the same as in Fig. 14. The animation can also be found at <https://youtu.be/Kwyp4Jvx6MU>. (<http://gji.oxfordjournals.org/lookup/suppl/doi:10.1093/gji/ggw329/-/DC1>)

Please note: Oxford University Press is not responsible for the content or functionality of any supporting materials supplied by the authors. Any queries (other than missing material) should be directed to the corresponding author for the paper.

## APPENDIX A: MELT-RELATED HEATING TERMS

As described in Section 2.1, we simplify the energy conservation equation (20), neglecting terms that include the melt velocity  $\mathbf{u}_f$ . This involves advective transport of heat by melt, adiabatic heating of melt, heating due to melt segregation and compression heating. These simplification lead to an energy equation (21) for a one-phase medium (also assuming no radiogenic heat production), but include latent heat of melting and freezing. Fig. A1 shows the differences between these two formulations at the example of a 1-D plume model. While differences between the heating rates due to adiabatic heating and dissipation heating are small, advection of heat by melt can significantly change the temperature distribution, leading to local temperature differences of more than 100 K at the top of the plume head.

## APPENDIX B: DERIVATION OF THE WEAK FORM

The weak form of the eqs (13)–(15) can be derived as follows. We multiply by test functions, integrate over the domain, and integrate by parts:

$$(2\eta\dot{\varepsilon}(\mathbf{u}_s), \dot{\varepsilon}(\mathbf{v}_s)) - \frac{2}{3}\eta(\nabla \cdot \mathbf{u}_s, \nabla \cdot \mathbf{v}_s) + (\nabla p_f, \mathbf{v}_s) + (\nabla p_c, \mathbf{v}_s) = (\bar{\rho}\mathbf{g}, \mathbf{v}_s), \quad (\text{B1})$$

$$(\nabla \cdot \mathbf{u}_s, q_f) - (\nabla \cdot K_D \nabla p_f, q_f) - \left( K_D \nabla p_f \cdot \frac{\nabla \rho_f}{\rho_f}, q_f \right) = -(\nabla \cdot (K_D \rho_f \mathbf{g}), q_f) + \left( \frac{1}{\rho_f} - \frac{1}{\rho_s} \right) (\Gamma, q_f) - \left( \frac{\phi}{\rho_f} \mathbf{u}_s \cdot \nabla \rho_f, q_f \right) - ((\mathbf{u}_s \cdot \mathbf{g})(1 - \phi)\kappa_s \rho_s, q_f) - (K_D \mathbf{g} \cdot \nabla \rho_f, q_f), \quad (\text{B2})$$

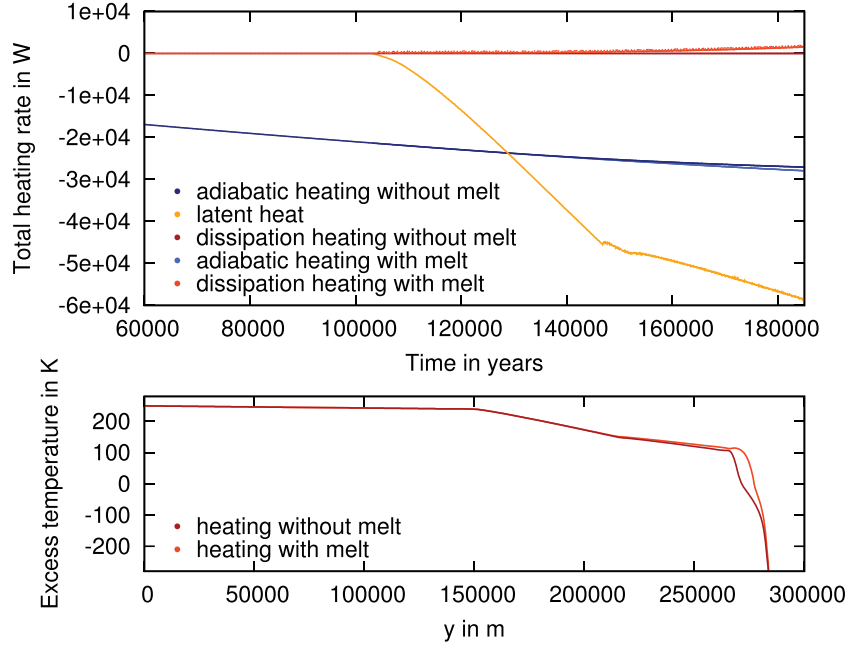


**Figure A1.** Comparison of the total heating rates (top) and temperature profiles (bottom) of 1-D plume models including and neglecting the effects of two-phase flow on heating and heat transport. The setup is the same as described in Section 4.1.

$$(\nabla \cdot \mathbf{u}_s, q_c) + \left( \frac{1}{\xi} p_c, q_c \right) = 0. \quad (\text{B3})$$

For the first equation we do integration by parts on the pressure terms ( $\mathbf{v} = 0$  on the boundary, so the boundary integral vanishes):

$$(2\eta \dot{\varepsilon}(\mathbf{u}_s), \dot{\varepsilon}(\mathbf{v}_s)) - \left( \frac{2}{3} \eta \nabla \cdot \mathbf{u}_s, \nabla \cdot \mathbf{v}_s \right) - (p_f, \nabla \cdot \mathbf{v}_s) - (p_c, \nabla \cdot \mathbf{v}_s) = (\bar{\rho} \mathbf{g}, \mathbf{v}_s). \quad (\text{B4})$$

We aim to include only material properties and not their derivatives in the equations, because these material descriptions are provided by ASPECT's user-defined plugins, which are designed to be easily comprehensible and extensible. Thus, we integrate the first part on the right hand side of the second equation by parts (and pick up a boundary term on  $\partial\Omega$ ):

$$(\nabla \cdot (K_D \rho_f \mathbf{g}), q_f) = - (K_D \rho_f \mathbf{g}, \nabla q_f) + \int_{\partial\Omega} q_f K_D \rho_f \mathbf{g} \cdot \bar{\mathbf{n}} \, ds.$$

We reverse the sign to later have a symmetric system:

$$\begin{aligned} -(\nabla \cdot \mathbf{u}_s, q_f) + (\nabla \cdot K_D \nabla p_f, q_f) + \left( K_D \nabla p_f \cdot \frac{\nabla \rho_f}{\rho_f}, q_f \right) &= - (K_D \rho_f \mathbf{g}, \nabla q_f) + \int_{\partial\Omega} q_f K_D \rho_f \mathbf{g} \cdot \bar{\mathbf{n}} \, ds \\ &\quad - \left( \frac{1}{\rho_f} - \frac{1}{\rho_s} \right) (\Gamma, q_f) + \left( \frac{\phi}{\rho_f} \mathbf{u}_s \cdot \nabla \rho_f, q_f \right) \\ &\quad + ((\mathbf{u}_s \cdot \mathbf{g})(1 - \phi) \kappa_s \rho_s, q_f) + (K_D \mathbf{g} \cdot \nabla \rho_f, q_f). \end{aligned} \quad (\text{B5})$$

The second term on the left needs to be integrated by parts to get

$$(\nabla \cdot K_D \nabla p_f, q_f) = - (K_D \nabla p_f, \nabla q_f) + \int_{\partial\Omega} q_f K_D \nabla p_f \cdot \bar{\mathbf{n}} \, ds.$$

We can use the boundary integral to prescribe Neumann boundary conditions for  $p_f$  (eq. 17), and with  $\nabla p_f = \mathbf{f}_2$  on the boundary we can move the boundary term to the right-hand side and get:

$$\int_{\partial\Omega} q_f K_D \rho_f \mathbf{g} \cdot \bar{\mathbf{n}} \, ds - \int_{\partial\Omega} q_f K_D \nabla p_f \cdot \bar{\mathbf{n}} \, ds = \int_{\partial\Omega} q_f K_D (\rho_f \mathbf{g} - \mathbf{f}_2) \cdot \bar{\mathbf{n}} \, ds.$$

For the third equation we also flip the sign to get

$$-(\nabla \cdot \mathbf{u}_s, q_c) - \left( \frac{1}{\xi} p_c, q_c \right) = 0. \quad (\text{B6})$$

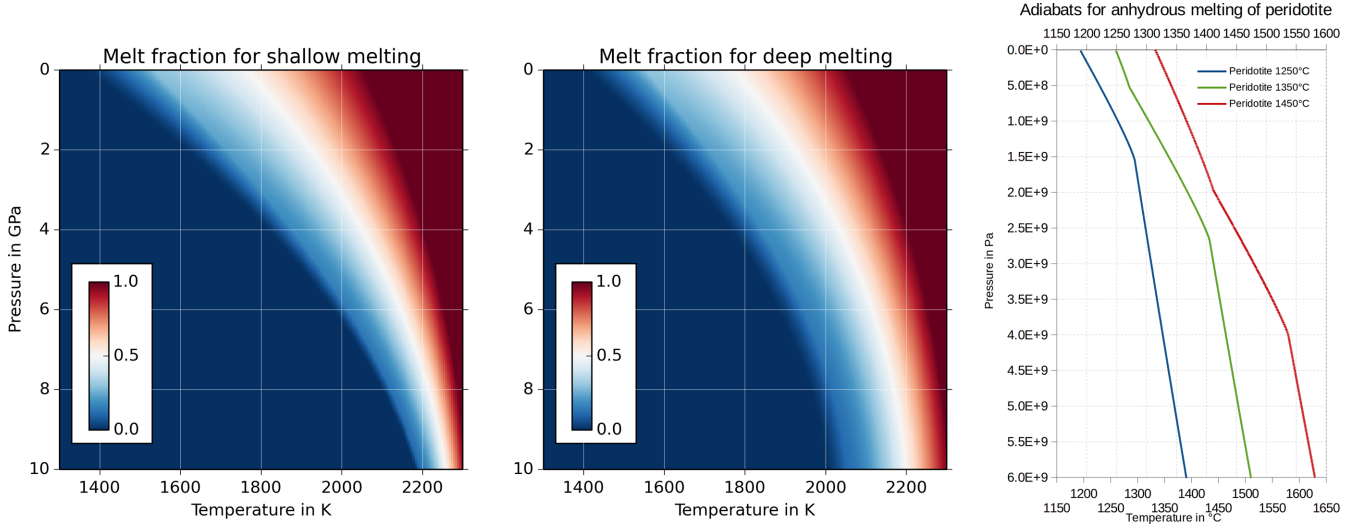


**Figure C1.** Melt fraction in dependence of temperature and pressure after Katz *et al.* (2003, left) and modified for deep melting (middle), and temperature profile of adiabatically upwelling material when latent heat of melting is taken into account for batch melting of anhydrous peridotite. Parametrizations after Katz *et al.* (2003).

## APPENDIX C: PARAMETRIZATION OF THE MELTING MODEL

Modelling of melt generation requires a parametrization for the melting rate in dependence of temperature, pressure and composition. We use the parametrization from Katz *et al.* (2003) for melting of dry peridotite (Fig. C1).

In addition, when material undergoes the phase transition from solid to fluid (or the other way round), latent heat is consumed (or released) proportional to the melting rate  $\Gamma = \rho_s \frac{DF}{Dt}$ . The effects of latent heat are included in the energy conservation equation in form of the term  $\rho_s T \Delta S \left( \frac{\partial F}{\partial t} + \mathbf{u}_s \cdot \nabla F \right)$ . Here,  $\Delta S$  is the change of entropy (positive for exothermic phase transitions) and  $F$  is the degree of depletion (the fraction of the source rock that has already been molten; without melt extraction from the source this is equal to the melt fraction). As the phase of the material, for a given composition, depends on the temperature and pressure, the latent heat term can be reformulated:

$$\begin{aligned} \frac{\partial F}{\partial t} + \mathbf{u}_s \cdot \nabla F &= \frac{DF}{Dt} \\ &= \frac{\partial F}{\partial T} \frac{DT}{Dt} + \frac{\partial F}{\partial p_s} \frac{Dp_s}{Dt} \\ &= \frac{\partial F}{\partial T} \left( \frac{\partial T}{\partial t} + \mathbf{u}_s \cdot \nabla T \right) + \frac{\partial F}{\partial p_s} \mathbf{u}_s \cdot \nabla p_s. \end{aligned}$$

The last transformation results from the assumption that the flow field is always in equilibrium and consequently  $\partial p / \partial t = 0$ . This means, we have to calculate the partial derivatives of our melt fraction parametrization with respect to temperature and pressure.

### C1 Melting of peridotite prior to the exhaustion of clinopyroxene

For peridotite, there are two different functions prior to and after the exhaustion of clinopyroxene. Prior to the exhaustion of clinopyroxene

$$\begin{aligned} F(p, T) &= \left( \frac{T - T_{\text{sol}}(p)}{T_{\text{liq}}^{\text{lh}}(p) - T_{\text{sol}}(p)} \right)^{\beta} \\ \frac{\partial F(p, T)}{\partial T} &= \beta \left( \frac{T - T_{\text{sol}}(p)}{T_{\text{liq}}^{\text{lh}}(p) - T_{\text{sol}}(p)} \right)^{\beta-1} \frac{1}{T_{\text{liq}}^{\text{lh}}(p) - T_{\text{sol}}(p)} \\ \frac{\partial F(p, T)}{\partial p} &= \beta \left( \frac{T - T_{\text{sol}}(p)}{T_{\text{liq}}^{\text{lh}}(p) - T_{\text{sol}}(p)} \right)^{\beta-1} \left( \frac{\partial T_{\text{liq}}^{\text{lh}}(p)}{\partial p} (T_{\text{sol}}(p) - T) + \frac{\partial T_{\text{sol}}(p)}{\partial p} (T - T_{\text{liq}}^{\text{lh}}(p)) \right) \frac{1}{(T_{\text{liq}}^{\text{lh}}(p) - T_{\text{sol}}(p))^2} \end{aligned}$$

with the solidus  $T_{\text{sol}}(p) = A_1 + A_2 p + A_3 p^2$ , the lherzolite liquidus  $T_{\text{liq}}^{\text{lh}}(p) = B_1 + B_2 p + B_3 p^2$  and the true liquidus  $T_{\text{liq}}(p) = C_1 + C_2 p + C_3 p^2$ .

**Table C1.** Parameters used for melting of anhydrous peridotite. Modified from Katz *et al.* (2003).

Parameter	Used for	Value	Value for deep melting	Unit
$A_1$	$T_{\text{sol}}$	1085.7	1120.7	K
$A_2$		$1.329 \times 10^{-7}$	$1.1 \times 10^{-7}$	$\text{K Pa}^{-1}$
$A_3$		$-5.1 \times 10^{-18}$	$-5 \times 10^{-18}$	$\text{K Pa}^{-2}$
$B_1$	$T_{\text{liq}}^{\text{lh}}$	1475.0		K
$B_2$		$8.0 \times 10^{-8}$		$\text{K Pa}^{-1}$
$B_3$		$-3.2 \times 10^{-18}$		$\text{K Pa}^{-2}$
$C_1$	$T_{\text{liq}}$	1780.0		K
$C_2$		$4.5 \times 10^{-8}$		$\text{K Pa}^{-1}$
$C_3$		$-2.0 \times 10^{-18}$		$\text{K Pa}^{-2}$
$\beta$	F	1.5		
$M_{\text{cpx}}$		0.15		mass fraction
$r_0$		0.5		mass fraction
$r_1$		$8 \times 10^{-11}$		mass fraction $\text{Pa}^{-1}$
$\Delta S$	Latent heat	-300		$\text{J kg}^{-1} \text{K}^{-1}$

## C2 Melting of peridotite after the exhaustion of clinopyroxene

The exhaustion of clinopyroxene happens at the melt fraction

$$F_{\text{cpx-out}} = \frac{M_{\text{cpx}}}{R_{\text{cpx}}(p)} \quad \text{with} \quad R_{\text{cpx}}(p) = r_0 + r_1 p$$

and marks a change in the productivity of the system.  $M_{\text{cpx}}$  is the mass fraction of clinopyroxene in the peridotitic host rock and  $R_{\text{cpx}}$  is the reaction coefficient for cpx in the melting reaction. For  $F > F_{\text{cpx-out}}$

$$F(p, T) = F_{\text{cpx-out}} + (1 - F_{\text{cpx-out}}) \left( \frac{T - T_{\text{cpx-out}}(p)}{T_{\text{liq}}(p) - T_{\text{cpx-out}}(p)} \right)^\beta$$

$$\frac{\partial F(p, T)}{\partial T} = \beta(1 - F_{\text{cpx-out}}) \left( \frac{T - T_{\text{cpx-out}}(p)}{T_{\text{liq}}(p) - T_{\text{cpx-out}}(p)} \right)^{\beta-1} \frac{1}{T_{\text{liq}}(p) - T_{\text{cpx-out}}(p)}$$

$$\begin{aligned} \frac{\partial F(p, T)}{\partial p} &= \frac{\partial F_{\text{cpx-out}}}{\partial p} \left[ 1 - \left( \frac{T - T_{\text{cpx-out}}(p)}{T_{\text{liq}}(p) - T_{\text{cpx-out}}(p)} \right)^\beta \right] + \beta(1 - F_{\text{cpx-out}}) \left( \frac{T - T_{\text{cpx-out}}(p)}{T_{\text{liq}}(p) - T_{\text{cpx-out}}(p)} \right)^{\beta-1} \\ &\quad \times \frac{\frac{\partial F_{\text{cpx-out}}}{\partial p} (T_{\text{cpx-out}}(p) - T_{\text{liq}}(p)) + \left( \frac{\partial T_{\text{liq}}}{\partial p} - \frac{\partial T_{\text{cpx-out}}}{\partial p} \right) (T_{\text{cpx-out}}(p) - T)}{(T_{\text{liq}}(p) - T_{\text{cpx-out}}(p))^2} \end{aligned}$$

$$\text{with } T_{\text{cpx-out}} = F_{\text{cpx-out}}^{\frac{1}{\beta}} [T_{\text{liq}}^{\text{lh}}(p) - T_{\text{sol}}(p)] + T_{\text{sol}}(p).$$

## C3 Parameters

The parameters used for the solidus and liquidus temperatures and the melt fraction are taken from Katz *et al.* (2003) for the case of anhydrous melting and are given in Table C1. For modelling melting under higher pressures, such as shown in Section 4.6 (deep melting), we modified the solidus temperature (reflecting a compositional change or change in volatile fraction), resulting in the deepest melts in the plume being generated in approximately 230 km depth.

## C4 Validation

We test our melting model by computing the numerical solution for the temperature profile of adiabatically upwelling material that undergoes melting and the associated latent heat effects. Fig. C1 (right) shows these results, which can be compared to equivalent data for anhydrous melting in Katz *et al.* (2003, fig. 11b), who calculate a simplified version of the productivity function

$$\left. \frac{dF}{dP} \right|_S = \frac{-\frac{c_p}{T} \frac{\partial T}{\partial P} \Big|_F + F \frac{\alpha_f}{\rho_f} + (1 - F) \frac{\alpha_s}{\rho_s}}{\Delta S + \frac{c_p}{T} \frac{\partial T}{\partial P} \Big|_P} \quad (\text{C1})$$

and then numerically integrate

$$\left. \frac{dT}{dP} \right|_S = \frac{T}{c_p} \left( F \frac{\alpha_f}{\rho_f} + (1 - F) \frac{\alpha_s}{\rho_s} + \Delta S \left. \frac{dF}{dP} \right|_S \right) \quad (\text{C2})$$

to receive the P-T path of the adiabat.